Electrostatic co-assembly of nanoparticles with oppositely charged small molecules into static and dynamic superstructures

Electrostatic co-assembly of nanoparticles with oppositely charged small molecules into static and dynamic superstructures

Tong Bian[1], Andrea Gardin[2,3], Julius Gemen[1], Lothar Houben[4], Claudio Perego[2], Byeongdu Lee[5], Nadav Elad[4], Zonglin Chu[1], Giovanni M. Pavan[2,3] and Rafal Klajn[1]*

[1]Department of Organic Chemistry, Weizmann Institute of Science, Rehovot 76100, Israel
[2]Department of Innovative Technologies, University of Applied Sciences and Arts of Southern Switzerland, CH-6928 Manno, Switzerland
[3]Department of Applied Science and Technology, Politecnico di Torino, 10129 Torino, Italy
[4]Department of Chemical Research Support, Weizmann Institute of Science, Rehovot 76100, Israel
[5]X-ray Science Division, Advanced Photon Source, Argonne National Laboratory, Lemont, IL 60439, USA
*e-mail: rafal.klajn@weizmann.ac.il

Coulombic interactions can be used to assemble charged nanoparticles into higher-order structures, but the process requires oppositely charged partners that are similarly sized. The ability to mediate the assembly of such charged nanoparticles using structurally simple small molecules would greatly facilitate the fabrication of nanostructured materials and harnessing their applications in catalysis, sensing, and photonics. Here we show that small molecules having as few as three charges can effectively induce attractive interactions between oppositely charged nanoparticles in water. These interactions can guide the assembly of charged nanoparticles into colloidal crystals of a quality previously only thought to result from their co-crystallization with oppositely charged nanoparticles of a similar size. Transient nanoparticle assemblies can be generated using positively charged nanoparticles and multiply charged anions that are enzymatically hydrolyzed into mono- and/or dianions. Our findings demonstrate an approach for the facile fabrication, manipulation, and further investigation of static and dynamic nanostructured materials in aqueous environments.

In one of its definitions, nanochemistry[1,2] focuses on the intriguing and diverse analogies between molecular-scale and nanosized species. In a widely cited example, ligand-protected metallic nanoclusters exhibit quantized energy levels and are often referred to as "superatoms"[3]. Larger, superparamagnetic and superferromagnetic nanoparticles (NPs) behave in many ways like atoms of paramagnetic and ferromagnetic metals, respectively[4,5]. Various ways of encoding "valency" in spherical NPs have been proposed[6] and utilized for constructing "colloidal molecules"[7]. NPs can also be assembled into one-dimensional structures in a process similar to the polymerization of small molecules[8]; indeed, the ability to visualize NPs by electron microscopy has been utilized to validate theoretical models developed for molecular polymerization. This analogy was further extended to copolymerization[9] and arresting polymerization with chain stoppers[10]. NPs have also been assembled into three-dimensional materials (colloidal crystals, or "supracrystals") with structures mimicking those of inorganic solids as simple as AlB_2 or NaCl[11], as well as ones without known molecular-scale analogs[12]. NP analogs of alloys and intermetallic compounds have been reported[13] and very small NPs within binary assemblies have been shown to behave as nanoscale electron equivalents[14]. Furthermore, analogies between molecular-scale and nanosized species extend to chemical reactions[15]. Similar to molecules, NPs can react with themselves[16], be subjected to oxidation[17], cation[18] and anion[19] exchange, and to other, more complex reactions, such as galvanic replacement[20]. Sequential reactions are possible[21,22] and the concept of the total synthesis of inorganic nanostructures has been proposed[23].

Similarly, spherical NPs functionalized with multiple charged groups (typically COO^- and NMe_3^+) behave in many ways like nanoscale analogs of simple ions[24,25]. These "superions" can attract each other and precipitate from solution as electroneutral solids, analogously to simple inorganic salts, such as AgI. There are, however, some notable differences between the behavior of small ions and charged nanoscale species. Figure 1a (left) shows an illustrative titration curve for the titration of Ag^+ with I^-, whereby precipitation occurs quickly when the solubility product, $K_{sp} = [A^+][B^-]$, is reached. In contrast, the titration of positively charged NPs with negatively charged ones leads to a gradual increase in the NP aggregate size[26] until precipitation occurs at a point of electroneutrality (i.e., the number of positively charged ligands on the added NPs reaches the number of negatively charged ligands on the titrated ones). Further addition of the negatively charged NPs leads to dissolution of the precipitate and the formation of increasingly smaller NP aggregates (Fig. 1a, *right*), which is not observed for small, non-complexing anions.

Interactions between oppositely charged small ions (e.g., Ag^+ and I^-) and, more recently, between oppositely charged nanosized species[24,25,27-29] have been investigated extensively. In contrast, relatively little attention has been devoted to studying electrostatic interactions across length scales, i.e., between charged NPs and small molecules bearing opposite charges. Here, we investigated the ability of small-molecule ions to mediate attractive interactions between oppositely charged NPs. Importantly, we found that a sharp transition between non-mediators and mediators occurs between doubly and triply charged molecules. Taking advantage of this finding, we prepared a family of colloidal crystals and developed a dissipative self-assembly system whereby NPs exist in the assembled state only during a continuous application of an oligoanion stimulus.

Results and discussion

Interactions between positively charged nanoparticles and small anions

A fundamental question to address when considering interactions between oppositely charged NPs and molecules is: What is the minimum number of charges on a small molecule required to induce attractive interactions with—and consequently, mediate the self-assembly of—oppositely charged NPs in water? To this end, we synthesized differently sized spherical gold NPs decorated with the positively charged trimethylammonium groups (TMA in Fig. 1b) and studied their interactions with simple anions comprising increasing numbers of negative charges. Irrespective of the diameter of the metallic core (we worked with NPs of various sizes between 2.8 nm and 13.1 nm Au NPs), the particles exhibited excellent solubility in water (with Br^- as the counterion; Fig. 1b, inset), as reported previously[24,30]. The colloidal stability of these NPs was not affected by the addition of aqueous solutions of various doubly charged anions (we tested carbonate CO_3^{2-}, sulfate(VI) SO_4^{2-}, hydrogen phosphate(V) HPO_4^{2-}, chromate(VI) CrO_4^{2-}, tartrate, and oxalate; all at pH values greater than pK_{a2}, to ensure double deprotonation), even when used in a 100-fold excess with respect to NP-bound TMA groups. In sharp contrast, all triply charged anions tested, including citrate, trimetaphosphate, and triply deprotonated ethylenediaminetetraacetic acid ($EDTA^{3-}$), caused a red-shift of the NPs' localized surface plasmon resonance (SPR) band, indicative of NP aggregation. Aggregation was also induced by anions featuring greater numbers of negative charges, including fully deprotonated EDTA ($EDTA^{4-}$), pyrophosphate $P_2O_7^{4-}$, triphosphate $P_3O_{10}^{5-}$, and hexametaphosphate $(PO_3)_6^{6-}$ (see Supplementary Fig. 4 for structural formulas). In all cases, aggregation was confirmed by transmission electron microscopy (TEM), which showed the formation of mostly amorphous NP aggregates (Supplementary Fig. 6).

To better understand these results, we performed molecular simulations of TMA-coated NPs interacting with HPO_4^{2-} and citrate as model doubly and triply charged anions, respectively (for details, see Supporting Information, Section 4). First, we studied the interactions between a positively charged NP surface and individual anions by all-atom molecular dynamics (AA-MD) simulations (Fig. 2a-b). To this end, we simulated a NP hemisphere (d = 7.4 nm) decorated with 347 TMA ligands (with Cl^- as the counterions) in the presence of citrate^{3-}, HPO_4^{2-}, or an extra Cl^- ion (each neutralized with three, two, or one Na^+ counterions, respectively). We investigated the interactions between the positively charged NP surface and individual anions by all-atom metadynamics (AA-MetaD) simulations[31-33] (Fig. 2a-b). During these simulations, the anions bound to and unbound from the NP surface multiple times (Fig. 2a), which allowed us to retrieve the free-energy profiles for their interaction with the NP (Fig. 2b). The minima at $d \approx 5$ Å are indicative of attractive interactions of all three anions with the NP-bound ligands, with the depth of the minimum proportional to the interaction free energy. We found that the difference in the interaction energy is proportional to the ionic valence, within the precision of the AA-MetaD technique (ΔG, ~2.7 kcal/mol for Cl^-, ~3.9 kcal/mol for HPO_4^{2-}, and ~6.1 kcal/mol for citrate^{3-}; yellow, blue, and red curves, respectively).

Next, we studied the ability of HPO_4^{2-} and citrate to mediate attractive interactions between two TMA-coated Au NPs (Supporting Information, Section 4.1). In these AA-MetaD simulations, 10 citrate^{3-} or 15 HPO_4^{2-} (neutralized by 30 Na^+) were placed between two NP halves, each decorated with 347 TMA groups (with the same number of Cl^- ions). Throughout these simulations, the distance between the NPs was varied repeatedly, allowing us to estimate the free energy of the NP–NP interaction as a function of NP–NP separation (Supplementary Fig. 9). With citrate, the free-energy profile extracted from the AA-MetaD simulation exhibited a minimum at the NP center-to-center distance of ~9.4 nm, indicating that the NPs have a tendency to assemble. However, upon replacing citrate with HPO_4^{2-}, this energy minimum disappeared and the global energy minimum moved toward larger distances (>10.5 nm), corresponding to the disassembled state (Supplementary Fig. 9b).

To model the anion-mediated self-assembly of positively charged NPs on a larger scale, we utilized coarse-grained molecular dynamics (CG-MD) simulations (see Supporting Information, Section 4.2). Figure 2c shows snapshots from CG-MD simulations of two TMA-coated Au NPs, each decorated with 804 TMA residues, neutralized by the corresponding number of HPO_4^{2-} or citrate^{3-} anions (804 and 536, respectively). Whereas both anions exhibited a strong affinity to the NPs, only citrates had the ability to bring the particles together during the CG-MD runs. This conclusion is also evident from Fig. 2d, where we plotted the distance between the centers of mass of the two NPs as a function of the CG simulation time.

To gain further insight into the NP aggregation behavior, we titrated suspensions of TMA-coated Au NPs (i.e., Au·TMA) in water with an aqueous solution of another trianion, namely, triply deprotonated EDTA (Fig. 1c) and followed the change in the position of Au NPs' SPR band, λ_{SPR}. Initially, λ_{SPR} corresponds to ~520 nm, typical of non-interacting NPs; a red-shift of the SPR band is indicative of NP aggregation. We found that upon the addition of EDTA^{3-}, λ_{SPR} red-shifts following a sigmoidal curve, and then stabilizes upon the addition of ~0.5 eq of EDTA^{3-} with respect to TMA groups (Fig. 1d), which corresponds to ~150% of the amount expected to achieve the electroneutrality point. No further changes were observed with higher amounts of the titrant (Fig. 1d). This aggregation profile is akin to that of the precipitation of a water-insoluble inorganic salt (Fig. 1a, *left*).

Our results are consistent with the Schulze–Hardy rule[34,35], which states that the ability of an electrolyte to mediate interactions between—and induce coagulation of—charged colloids is

proportional to the electrolyte's ionic valence, z. Specifically, the critical coagulation concentration, CCC, scales with z as CCC $\propto z^{-6}$, indicating that a small increase in charge can greatly increase the ion's potency to trigger coagulation[36]. For example, increasing the charge from –2 (for HPO_4^{2-}) to –3 (for citrate^{3-}) decreases the CCC value by as much as ~11-fold. In other words, the assembly of Au·TMA would require a much higher concentration of HPO_4^{2-} than of citrate^{3-}. However, at this high concentration, the ionic strength of the solution is high enough to screen the electrostatic interactions; hence, the assembly of Au·TMA using divalent (or monovalent) anions is never observed.

The Schulze–Hardy rule states that CCC is sensitive to the number of charges on the electrolyte, but not to the way these charges are distributed across the anion. We hypothesized that flexible anions might be more potent in mediating the self-assembly of TMA-coated Au NPs. To address this question, we titrated 5.2 nm Au·TMA with three different tricarboxylates, differing only in the number of methylene groups: propane-1,2,3-tricarboxylate, butane-1,2,4-tricarboxylate, and pentane-1,3,5-tricarboxylate (Supporting Information, Section 5). These experiments showed no appreciable difference in the behavior of the titrant (Supplementary Fig. 15). We also worked with a significantly more rigid benzene-1,3,5-tricarboxylate, only to find that the titration profile remained the same. Based on these results, we conclude that the conformational flexibility of oligoanions has little effect on their propensity to mediate the assembly of positively charged NPs, at least in this series.

To further demonstrate the importance of Coulombic interactions in our system, we prepared aqueous suspensions of differently sized Au·TMA (4.8 nm, 8.8 nm, and 13.1 nm) and titrated them with the same solution of EDTA^{3-} (Extended Data Fig. 1). If the contribution of van der Waals (vdW) interactions to the formation of NP aggregates was significant, the largest NPs would aggregate first, followed by the 8.8 nm and 4.8 nm NPs. We found, however, that the aggregation profiles for all three NP sizes were practically the same, indicating that the interparticle interactions in our system are governed predominantly by electrostatics.

Remarkably, reversing the order of titration resulted in a drastically different NP aggregation behavior. When an aqueous solution of EDTA^{3-} was titrated with Au·TMA in water, the added NPs assembled into increasingly large aggregates, which subsequently decreased in size upon the continued addition of the NPs, eventually resulting in a suspension of non-interacting NPs (Fig. 1e). This aggregation/disaggregation profile is reminiscent of that previously observed for mixtures of positively and negatively charged NPs (Fig. 1a, *right*). Interestingly, however, the highest degree of aggregation was consistently observed after the addition of only one-third of the NPs required to achieve electroneutrality (denoted by a dashed red line in Fig. 1e, *right*; note the position of the maximum with respect to the line). Overall, our results indicate that i) the yield of electroneutral aggregates comprising "superions" and small-molecule counterions is maximized in the presence of an excess of the latter, which can be attributed to the entropic penalty associated with bringing multiple small ions together, and ii) once formed, these electroneutral aggregates can be disassembled with an excess of "superions", but not molecular-scale ions, thus combining the characteristics of a molecular-scale system (ionic aggregates; Fig. 1a, *left*) and a nanoscale system (aggregates of opposite charged NPs; Fig. 1a, *right*).

Dynamics of small ions within nanoparticle/molecule ionic aggregates and their structural transformation into crystalline assemblies

The CG-MD simulation described above demonstrates that citrate ions can readily mediate attractive interactions between two positively charged TMA-coated NPs (Fig. 2c). Next, we investigated the mobility of citrates within the resulting ensemble of two bound Au·TMA NPs. To this end, we

extended the CG-MD simulation and analyzed the trajectory covering the period from 0.9 μs (i.e., once the NPs have stably aggregated; see Fig. 2c, d) to 8.4 μs. We turned to machine learning in order to study the variability of the arrangement of citrates in the system. We used an unsupervised clustering method—specifically, the Probabilistic Analysis of Molecular Motifs (PAMM)[37]—employing the Smooth Overlap of Atomic Positions (SOAP)[38] as rich descriptors of the molecular environment surrounding each citrate in the molecular model. Such an analysis allows the classification of different citrates based on differences in the local environment that surrounds them during the CG-MD (namely, pertaining to local order, persistency in the interactions, etc.) to follow the local variations and fluctuations in the citrate states and also to reconstruct the dynamic mobility of the citrates in different regions of the system[39]. The analysis subdivides the citrates in the system into three distinct clusters (states): i) citrates located at the interface between the two NPs (red in Fig. 3a), ii) citrates interacting with a single NP (gray), and iii) an intermediate state between the first two (green) (for details, see Supporting Information, Section 4.2.2). The movement and reshuffling of citrates between the three clusters during the CG-MD reveal the dynamics between the states (Fig. 3a, left vs. right).

From the CG-MD trajectory, we also constructed a two-dimensional free-energy surface (FES) of the citrates in the system (Fig. 3b), represented as a function of two variables (the contact variable, *CONT*, describing the number of contacts with NP-adsorbed TMA ligands, and the distance variable, *DIST*, describing the position of a citrate on the NP cluster; Supplementary Fig. 13). This analysis identified three local free-energy minima in the FES (Fig. 3b), consistent with the above unsupervised clustering classification obtained above.

By tracking the individual citrates during the CG-MD simulation, we could monitor their transition probabilities between the three states. Such probabilities, obtained by computing the transition matrix among the three different states from the clustering analysis of the CG-MD (see Supplementary Fig. 12d), are reported next to the arrows inside the FES in Fig. 3b. These transition probabilities are extracted from a simplified CG model, and thus have a qualitative value; nonetheless, they are comparable to one another and are proportional to the rate constants of citrates in one state transitioning to another. Moreover, we computed the mean square displacement of citrates in different clusters (Supplementary Fig. 14), which, even accounting for simplifications in the model, allowed us to estimate the diffusion of the "gray" citrates across the NP surface as being ~1 order of magnitude faster than of the more static "red" citrates. Thus, these results demonstrate the internal dynamics of the system, where the citrates at the interface between two bound NPs are less dynamic (but not completely static) than those bound to the surface of a single NP.

We hypothesized that the facile diffusion of oligoanions between positively charged NPs, as revealed by the MD simulations, might facilitate the transformation of the initial, mostly amorphous aggregates into regular, crystalline assemblies (which represent the thermodynamic minimum of the system). Indeed, we found that when left undisturbed in an aqueous suspension at room temperature, the Au·TMA/citrate precipitates developed multiple crystalline domains over the course of 24 h (Fig. 3c, *bottom*). At an elevated temperature (50 ºC), the "annealing" process was complete within 1 h and resulted in colloidal crystals 200–300 nm across, which did not grow further (Fig. 3d). Overall, the observed increase in the NP order within the Au·TMA/citrate aggregates supports the idea of the oligoanions acting as a dynamic—as opposed to "frozen"—ionic glue.

To characterize the crystalline assemblies, we utilized cryogenic TEM (cryo-TEM) – a technique that preserves the native (solution) structures during imaging. However, cryo-TEM requires that the specimens be very thin – we thus attempted to image aggregates obtained immediately after treating the TMA-coated Au NPs with an oligoanion (here, $P_3O_{10}^{5-}$). Interestingly, whereas these aggregates

appeared amorphous at a low magnification (Fig. 3e), close inspection revealed that they were composed of small (~20–50 nm) interconnected aggregates featuring a regular arrangement of NPs; thus, they exhibited a short-range crystalline order. In particular, we observed multiple instances of ~25 nm aggregates that we identified by cryo-scanning TEM (cryo-STEM) tomography as Mackay icosahedra[40] (Fig. 3f). Within these aggregates, the central NP is surrounded by a 12-NP icosahedral shell, which is enclosed inside an outer, deltahedral shell composed of 42 NPs, giving rise to a closed-shell, "magic number" cluster consisting of 55 NPs. The formation of clusters that maximize packing density of like-charged NPs may seem surprising, but is enabled by the presence of small, oppositely charged molecules that compensate for the electric charges on the NPs. Based on our tomography results, we determined the nearest-neighbor distance within the Mackay icosahedron (Fig. 3f) as 8.1 nm. Given that the aggregate is composed of 4.73 nm NPs, the gap between the metallic cores is equal to 3.37 nm – slightly more than twice the length of a TMA ligand in its fully extended conformation (2 × 1.64 nm, which is the distance between the surface of Au and the terminal N atom), leaving enough space for a monolayer $P_3O_{10}^{5-}$ anions.

Crystalline aggregates of oppositely charged nanoparticles and small ions

We hypothesized that the attractive electrostatic interactions between positively charged NPs and oligoanions could be used for constructing large colloidal crystals ("supracrystals"), and ultimately nanostructured materials. Since the annealing experiments shown in Fig. 3c-d did not afford crystalline domains larger than ~300 nm, we sought another method to prepare crystalline assemblies of our NPs. A previously reported method of generating ordered assemblies of ionic NPs is based on i) generating amorphous aggregates by electrostatic interactions between oppositely charged nanosized entities, ii) adding an inorganic salt (typically NaCl) at a high concentration to screen the electrostatic interactions and therefore, to disassemble the initial aggregates[41,42], and iii) slowly decreasing the ionic strength of the solution by dialysis against pure water. Although this strategy has been successfully applied to generate ordered assemblies of positively charged NPs and negatively charged DNA[43], it is not applicable to our system, where small-molecule anions would diffuse through the dialysis membrane and leave the solution, along with the screening agent. However, we hypothesized that this problem could be tackled by employing an intrinsically unstable screening agent that i) bears no more than two negative charges on the anion (to avoid mediating NP assembly) and ii) undergoes a spontaneous decomposition into non-ionic products, thus slowly reducing the ionic strength of the solution and triggering electrostatic interactions in the system. These criteria are met by ammonium carbonate, whose added benefit is that the decomposition products (NH_3 and CO_2) are gaseous and spontaneously leave the system[44]:

$$2\ NH_4^+ + CO_3^{2-} \rightarrow 2\ NH_3\uparrow + CO_2\uparrow + H_2O.$$

We were pleased to find that i) the addition of ammonium carbonate induced the redissolution of all the ion/superion precipitates described above (we worked with a concentrated $(NH_4)_2CO_3$ solution; $c \approx 2.5$ M), and ii) the spontaneous decomposition of $(NH_4)_2CO_3$ resulted in the formation of well-defined colloidal crystals (over the course of ~24 h) (Fig. 4a).

Figure 4b–h shows representative scanning electron microscopy (SEM) images of colloidal crystals comprising TMA-coated Au NPs and various multiply charged anions (for additional examples, see Extended Data Fig. 2 and Supporting Information, Section 6). Interestingly, the crystallinity of the assemblies was not compromised by the presence of relatively large uncharged moieties on the anions – for example, replacing triphosphate $P_3O_{10}^{5-}$ with adenosine triphosphate (ATP) resulted in crystals of the same quality (Supplementary Fig. 18). Irrespective of the anion and the NP size, the

NPs assembled into close-packed colloidal crystals whose average sizes could be controlled in the 1–50 μm range simply by tuning the concentration of NPs during crystallization between 0.16 and 10 mg/mL (Supplementary Figs. 17-18). The largest crystals were obtained from 4.7 nm Au·TMA as thin hexagonal plates with a diameter of >50 μm, which corresponds to as many as ~6000 NPs arranged regularly in a row; these crystals were sufficiently large to be imaged by optical microscopy (Fig. 4i). In terms of the number of repeating unit cells (>4000), they represent some of the highest-quality colloidal crystals from small NPs obtained to date. We believe that this long-range order is enabled by the mobility of the mediating oligoanions between the TMA-coated NPs (as revealed by the MD simulations). This mobility (particularly pronounced at the early stages of aggregation, when the ionic strength is still relatively high) can enable the NPs to adjust their positions and optimize the packing within the aggregate, ultimately resulting in a long-range, crystalline order.

Analysis of the SEM images revealed that irrespective of the oligoanion used, the colloidal crystals exhibited morphologies (habits) typical of atomic crystals with a face-centered cubic (*fcc*) lattice[45], including hexagonal plates (Fig. 4c) and truncated decahedra (Fig. 4e). Moreover, we directly observed the lowest-energy crystal facets of *fcc* lattices, namely, (111) and (100) (see Extended Data Fig. 3). To confirm the *fcc* structure, we analyzed colloidal crystals assembled from 4.73 nm Au·TMA and $P_3O_{10}^{5-}$ by synchrotron-based small-angle X-ray scattering (SAXS). Figure 4j shows a 1D SAXS pattern of an aqueous suspension of the colloidal crystals. Interestingly, repeated measurements on several samples of Au·TMA/$P_3O_{10}^{5-}$ crystals consistently revealed the presence of two types of *fcc* lattices (major and minor). The pink trace is a simulated pattern for an *fcc* crystal with a lattice constant, a = 121.3 Å that corresponds to the dominant structure. This value of a corresponds to the NP center-to-center distance of 8.58 nm; given the diameter of the metallic core = 4.73 nm and twice the TMA monolayer thickness (~1.64 nm; defined here as the distance between the NP surface and the terminal N atom) ≈ 3.28 nm, the gap between fully extended TMA ligands on the neighboring NPs ≈ 0.57 nm. We note that this value is slightly larger than the one within Mackay icosahedra (which were obtained from $P_3O_{10}^{5-}$ and the same batch of NPs); this small increase can be attributed to the larger interparticle distance within an *fcc* lattice compared to a densely packed icosahedral cluster.

For the minor *fcc* species simulated by the blue trace in Fig. 4j, we found that a = 130.9 Å. The two lattices coexisted throughout the aqueous suspension, although the relative intensities of their signals depended on the location within the sample. Interestingly, these results could be correlated with SEM imaging, which often showed a bimodal size distribution of the colloidal crystals. For example, Supplementary Fig. 19 shows a mixture of ~5 μm and ~20 μm crystals obtained after slow removal of $(NH_4)_2CO_3$ from the solution of 4.73 nm Au·TMA and $P_3O_{10}^{5-}$. We hypothesize that the small crystals might correspond to the minor (i.e., large-a) lattice found by SAXS, and the larger ones – to the major (small-a) one. We note that at the onset of crystallization, the solution contains a substantial amount of CO_3^{2-} and NH_4^+. Whereas the former ions are incapable of mediating attractive interactions between the NPs, the latter can readily interact with $P_3O_{10}^{5-}$ adsorbed onto TMA-coated NPs by means of both electrostatic and hydrogen-bonding interactions, resulting in the entrapment of NH_4^+ within the crystals, as schematically illustrated in Fig. 4k, *bottom* (indeed, the gap between extended TMA ligands in this large-a lattice ≈ 1.25 nm, i.e., it is slightly more than twice the gap in the small-a lattice). Over time, however, the amount of NH_4^+ in the system decreases, and the growth of these crystals is arrested at the expense of the small-a crystals illustrated in Fig. 4k, *top*.

We also investigated colloidal crystals composed of the same 4.73 nm NPs and ATP and similarly found the coexistence of a major species with a smaller a (119.8 Å) and a minor species with a larger a (130.9 Å) (Fig. 4l). The lattice constant for the major species corresponds to the interparticle gap (the distance between the terminal N atoms of fully extended TMAs) of ~0.46 nm. The smaller gap found

in the Au·TMA/ATP crystals (compare with ~0.57 nm for Au·TMA/ $P_3O_{10}^{5-}$) may seem surprising, given the significantly larger size of ATP compared with $P_3O_{10}^{5-}$ (which is essentially ATP lacking the nucleoside moiety). However, it is reasonable to hypothesize that the organic part of ATP might intercalate between the NP-adsorbed TMA ligands, thus strengthening the interactions within the Au·TMA/ATP aggregates.

Interactions between negatively charged nanoparticles and small cations

Next, we were interested in determining whether the observed behavior can be extended to a "reverse" system of negatively charged NPs and oligocations. To address this question, we synthesized i) 4.7 nm Au NPs coated with thiols terminated with sulfonate groups (MUS in Fig. 5a; note that we used sulfonate rather than carboxylate end groups in order to ensure a maximum degree of deprotonation[46]) and ii) small molecules bearing three and two positively charged quaternary ammonium groups (OMA^{3+} and HMA^{2+} in Fig. 5b). Upon the dropwise addition of an aqueous solution of OMA^{3+} to MUS-coated Au NPs (i.e., Au·MUS) in water, an S-shaped titration curve was observed (Fig. 5c), similar to the titration profile of Au·TMA with oligoanions. However, we consistently observed that a slight excess of OMA^{3+} (with respect to the amount of oligoanions used for titrating Au·TMA) had to be added to reach the curve's inflection point (denoted by the dashed red line in Fig. 5c; compare with Fig. 1d for $EDTA^{3-}$). As expected, the control dication HMA^{2+} did not mediate interactions between Au·MUS (Fig. 5c), even when used in a large excess (Supplementary Fig. 21).

Similarly, titrating a solution of OMA^{3+} with Au·MUS afforded NP aggregates, which gradually disassembled as more Au·MUS was added (Fig. 5d). The analogy to the original Au·TMA/oligoanions system could be extended further: upon increasing the ionic strength using $(NH_4)_2CO_3$, the Au·MUS/OMA^{3+} aggregates dissolved as the electrostatic interactions were screened; moreover, the slow decomposition of $(NH_4)_2CO_3$ that followed resulted in the formation of well-defined colloidal crystals (Fig. 5e-f and Extended Data Fig. 4).

Out-of-equilibrium aggregates of oppositely charged nanoparticles and small ions

The above results indicate that small anions bearing three (or more) negative charges can mediate attractive interactions between positively charged NPs, which remain unassembled in the presence of mono- or dianions. These findings led us to hypothesize that a spontaneous decrease in the charge of the "anionic glue" within the aggregates of Au·TMA should entail the disassembly of these aggregates. Such a charge reduction could occur as a result of the hydrolysis of multiply charged anions, which, owing to their high charge density, are often thermodynamically unstable and can be catalytically decomposed into smaller, mono- and di-anionic species. A prime example of such a process is ATP hydrolysis – a highly exergonic reaction catalyzed by phosphatase enzymes[47]. Therefore, we reasoned that in the presence of a phosphatase, ATP would act as a stimulus for the transient generation of NP aggregates (Fig. 6a).

The blue trace in Fig. 6c (labeled "start") shows a UV/Vis absorption spectrum of an aqueous solution of TMA-functionalized 7.4 nm Au NPs in the presence of a phosphatase enzyme, potato apyrase. The λ_{SPR} value of the solution is centered at 519 nm, indicating that the particles are well dispersed in the solution. Upon injection of an ATP aliquot, λ_{SPR} rapidly increased and stabilized (within 2 min) at ~565 nm, accompanied by a pronounced increase in absorbance at 800 nm (A_{800}) – i.e., changes indicative of NP aggregation. We were pleased to find that at $t \approx 60$ min, A_{800} started to

decrease sharply and the initial spectrum was regenerated within the next 20 min, indicating that the process is reversible. A similar assembly/disassembly profile was observed by dynamic light scattering (DLS), where the addition of ATP resulted in the rapid formation of ~90 nm aggregates, which persisted for ~100 min, and then disassembled within a relatively short period of time (Fig. 6d). SEM imaging revealed the amorphous nature and lack of long-range order within these aggregates (Fig. 6e; see also Supplementary Figs. 23-24 and TEM images in Supplementary Fig. 25).

The equilibrium state of our system corresponds to ATP hydrolyzed into adenosine monophosphate (AMP) and HPO_4^{2-}, neither of which induces the self-assembly of Au·TMA. However, because the ATP-induced self-assembly of NPs is faster than ATP hydrolysis, NP aggregates will exist temporarily—in the out-of-equilibrium regime—for as long as ATP is present at a sufficiently high concentration. Therefore, an assembly/disassembly cycle is associated with a chemical reaction involving the consumption of a high-energy species ("energy dissipation"), constituting an example of dissipative self-assembly (DSA).[48-52] DSA of NPs has previously been reported for silicon[53], gold[54], polystyrene[55] particles, however, in all cases self-assembly was triggered by small-molecule "fuels" that are not biocompatible.

To verify that the disassembly of NP aggregates was triggered by the enzymatic activity of apyrase, we worked with a non-hydrolyzable ATP analog, adenosine [β,γ-imido]-triphosphate (APPNP)[56] (Supplementary Fig. 4). We found that whereas APPNP induced NP aggregation similarly to ATP, the resulting aggregates showed no signs of the disassembly in the presence of the enzyme. Similarly, aggregates obtained from Au·TMA and other multiply charged anions—such as pyrophosphate and triphosphate—remained static in the presence of apyrase. At the same time, pyrophosphate and triphosphate can be hydrolyzed by another enzyme from the phosphatase family, namely, alkaline phosphatase (ALPase), which is not specific for ATP. Indeed, the addition of either $P_2O_7^{4-}$ or $P_3O_{10}^{5-}$ to an aqueous solution of Au·TMA in the presence of ALPase resulted in assembly, followed by disassembly – the latter not observed with apyrase.

Once the oligophosphate stimulus had been consumed and the system returned to its non-assembled, equilibrium state, a new assembly/disassembly cycle could be initiated by injecting a fresh aliquot of the stimulus (Fig. 6f). Remarkably, the optical properties and structure of the aggregates generated in the sixth cycle were indistinguishable from those obtained by the initial injection of ATP (Fig. 6f-g), although it took them ~3 times as long to disassemble completely (Fig. 6f; see also Supplementary Fig. 26). Differently sized NPs behaved similarly; see Supplementary Figs. 27-29. More than 20 assembly/disassembly cycles could be performed with TMA-functionalized Au NPs using various multiply charged oligophosphates. This high recyclability stands in sharp contrast to many other synthetic DSA systems, where only up to several cycles are typically observed[57-59]. In these previously reported systems, the chemical "waste" generated during the initial cycles often interferes with the assembly process. We attribute the comparatively excellent performance of our system to the non-invasive nature of the waste—AMP and HPO_4^{2-}—which, as dianions, are incapable of inducing NP aggregation. However, owing to the slightly weaker basicity of the "waste" anions, compared with the ATP stimulus, the solution pH drops when the number of assembly/disassembly cycles increases, which lowers the enzyme activity and therefore extends the lifetimes of the transient aggregates. Furthermore, repeated cycling results in a gradual increase in the ionic strength of the solution, which will ultimately prevent NP aggregation owing to the screening of electrostatic interactions between Au·TMA and the oligoanions.

Remarkably, we observed very different disassembly profiles for the aggregates of Au·TMA in the presence of ALPase, depending on the anion used (Fig. 6h). The addition of both adenosine triphosphate and inorganic triphosphate resulted in rapid aggregation of the NPs (Fig. 6h, t = 0–3

min). However, whereas Au·TMA/ATP aggregates persisted for a defined period of time, after which they rapidly disassembled, the disintegration of the aggregates obtained from $P_3O_{10}^{5-}$ began soon after they formed, proceeding at a steady rate until a solution of free NPs was regenerated after several hours (Fig. 6h; the solid triangles and empty circles, respectively). To better understand these results, we prepared both types of aggregates (Au·TMA/ATP and Au·TMA/ $P_3O_{10}^{5-}$) in the absence of the enzyme and compared their structures using cryo-TEM (to avoid artefacts resulting from sample drying). As mentioned above, Au·TMA/$P_3O_{10}^{5-}$ was composed of small, pseudospherical ~20–50 nm NP aggregates linked into larger, branched structures (Fig. 6i; see also Supplementary Fig. 39). The formation of such "aggregates of aggregates"[60-63] is not surprising, given that the mediating agent ($P_3O_{10}^{5-}$) was used in the amount necessary to compensate for the overall positive charge on the NPs. Surprisingly, however, analogous primary aggregates obtained using ATP persisted without aggregating further (Fig. 6j; see also Supplementary Fig. 40). We also analyzed both types of aggregates in more detail by cryo-STEM tomography (see Extended Data Figs. 5–7). This analysis revealed that i) the interparticle center-to-center distance within the Au·TMA/ATP aggregates is shorter than for the Au·TMA/$P_3O_{10}^{5-}$ aggregates (8.08 ± 0.07 nm vs. 8.27 ± 0.03 nm; in agreement with the SAXS results) and ii) the number of nearest NP neighbors is larger within the Au·TMA/ATP aggregates (7.4 ± 0.5, compare with 6.4 ± 0.8 for Au·TMA/$P_3O_{10}^{5-}$). Taken together, these results indicate that the Au·TMA/ATP aggregates have a more compact nature, which can be attributed to the incorporation of ATP's nucleoside group within the organic monolayer on the NPs (as discussed above in the context of the SAXS results). Importantly, such an intercalation would render Au·TMA/ATP aggregates less dynamic, which can explain both i) their resistance towards further aggregation and ii) their enhanced stability against enzymatic hydrolysis (i.e., any excess (unbound) ATP is consumed first; we note that the disassembly profile in Fig. 6h is remarkably similar to typical assembly profiles (e.g., Fig. 1d) analyzed backwards). In contrast, in the Au·TMA/$P_3O_{10}^{5-}$ system, the enzyme discriminates less between free and NP-bound $P_3O_{10}^{5-}$: both are consumed, which explains the disassembly profile shown in Fig. 6h.

Finally, we hypothesized that the lifetimes of the out-of-equilibrium NP aggregates could be controlled by the amount of added stimulus (green in Fig. 6d). Figure 6k shows the dependence of the λ_{SPR} value on Au·TMA following the addition of increasing amounts of ATP. The rapid disassembly of the NP aggregates commenced ~20 min after adding 13.5 nmol of ATP vs. as long as ~180 min after adding 40.5 nmol of the stimulus. The behavior of our system is reminiscent of the reversible formation of actin filaments[64], which similarly assemble (from a globular protein G-actin) in the presence of ATP. Within these assemblies, ATP is rapidly hydrolyzed[65], and they need to constantly be resupplied with ATP to remain in the assembled, out-of-equilibrium state. In addition, our system allows for an additional way of controlling the lifetimes of the dynamic NP aggregates, which is based on varying the concentration (activity) of the enzyme. As Fig. 6l shows, aggregates generated by the addition of 27 nmol ATP could persist for periods of ~5–200 min, depending on the concentration of apyrase (~3–22 units of the enzyme per mL).

Conclusions

In sum, we investigated electrostatic interactions across the molecular and nanoscopic length scales, focusing on a model system of negatively charged small molecules and positively charged nanoparticles. We found that small molecules having three (or more) charges could mediate attractive interactions between oppositely charged NPs, whereas those bearing one or two charges were unable to do so. These results could be rationalized by the Schulze–Hardy rule applied to a system of small NPs. Titration of charged NPs with oppositely charged small-molecule ions and vice versa demonstrated that our system combines the characteristics of molecular-scale and nanoscale systems,

depending on the order of addition. Molecular dynamics simulations revealed that oligoanions holding nanoparticles together behave like a "dynamic ionic glue", thus facilitating structural transformations of the NP aggregates. Our results indicate that co-crystallization of charged NPs with oppositely charged small molecules, over one order of magnitude smaller in size, can give rise to colloidal crystals of a quality previously only thought to arise from co-assembling oppositely charged entities of similar sizes. Based on the above findings, we conceived a dissipative self-assembly system, whereby NPs exist in the aggregated state only under a continuous supply of multiply charged anions, which are constantly hydrolyzed into smaller anions. These results open up several avenues for further research. First, we anticipate that the herein disclosed method for crystallizing NPs, based on the spontaneous decomposition of a volatile salt, will provide important insights into the underlying crystallization mechanisms. Second, the finding that the molecular ions within NP/ion aggregates exhibit mobility suggests that these aggregates may behave and will be investigated as ionic conductors. Third, it will be interesting to integrate metastable-state photoacids within our system of NP/trianion aggregates; the light-induced proton release can be used for protonating the trianion, thus reversibly toggling between a trianion (in the dark; induces NP aggregation) and a dianion (under light; no aggregation), and consequently disassembling and reassemling the NPs for multiple cycles. Finally, the ATP-mediated dissipative self-assembly system represents a unique example of a system composed of biocompatible components and one that operates in water, thus bringing us closer to interfacing dynamically self-assembling NPs with biological environments.

Data availability. All the data supporting the findings of this study are available within the main text of the paper and the Supporting Information and also from the corresponding author on request.

References

1. Sergeev, G. B. & Klabunde, K. J. *Nanochemistry*. 2nd edition (Elsevier, 2013).
2. Ozin, G. A., Arsenault, A. & Cademartiri, L. *Nanochemistry: A chemical approach to nanomaterials*. 2nd edition (RSC Publishing, 2008).
3. Walter, M. et al. A unified view of ligand-protected gold clusters as superatom complexes. *Proc. Natl. Acad. Sci. USA* **105**, 9157–9162 (2008).
4. Bedanta, S. & Kleemann, W. Supermagnetism. *J. Phys. D Appl. Phys.* **42**, 013001 (2009).
5. Morup, S., Hansen, M. F. & Frandsen, C. Magnetic interactions between nanoparticles. *Beilstein J. Nanotech.* **1**, 182–190 (2010).
6. Song, L. & Deng, Z. Valency control and functional synergy in DNA-bonded nanomolecules. *ChemNanoMat* **3**, 698–712 (2017).
7. Wei, Y., Bishop, K. J. M., Kim, J., Soh, S. & Grzybowski, B. A. Making use of bond strength and steric hindrance in nanoscale "synthesis". *Angew. Chem. Int. Ed.* **48**, 9477–9480 (2009).
8. Liu, K. et al. Step-growth polymerization of inorganic nanoparticles. *Science* **329**, 197–200 (2010).
9. Liu, K. et al. Copolymerization of metal nanoparticles: A route to colloidal plasmonic copolymers. *Angew. Chem. Int. Ed.* **53**, 2648–2653 (2014).
10. Klinkova, A., Thérien-Aubin, H., Choueiri, R. M., Rubinstein, M. & Kumacheva, E. Colloidal analogs of molecular chain stoppers. *Proc. Natl. Acad. Sci. USA* **110**, 18775–18779 (2013).
11. Shevchenko, E. V., Talapin, D. V., Kotov, N. A., O'Brien, S. & Murray, C. B. Structural diversity in binary nanoparticle superlattices. *Nature* **439**, 55–59 (2006).
12. Udayabhaskararao, T. et al. Tunable porous nanoallotropes prepared by post-assembly etching of binary nanoparticle superlattices. *Science* **358**, 514–518 (2017).
13. Wang, S. et al. Colloidal crystal "alloys". *J. Am. Chem. Soc.* **141**, 20443–20450 (2019).

14. Girard, M. et al. Particle analogs of electrons in colloidal crystals. *Science* **364**, 1174–1178 (2019).
15. Vasquez, Y., Henkes, A. E., Bauer, J. C. & Schaak, R. E. Nanocrystal conversion chemistry: A unified and materials-general strategy for the template-based synthesis of nanocrystalline solids. *J. Solid State Chem.* **181**, 1509–1523 (2008).
16. Krishnadas, K. R. et al. Interparticle reactions: An emerging direction in nanomaterials chemistry. *Acc. Chem. Res.* **50**, 1988–1996 (2017).
17. Yin, Y. et al. Formation of hollow nanocrystals through the nanoscale Kirkendall effect. *Science* **304**, 711–714 (2004).
18. Son, D. H., Hughes, S. M., Y., Y. & Alivisatos, A. P. Cation exchange reactions in ionic nanocrystals. *Science* **306**, 1009–1012 (2004).
19. Park, J., Zheng, H., Jun, Y.-w. & Alivisatos, A. P. Hetero-epitaxial anion exchange yields single-crystalline hollow nanoparticles. *J. Am. Chem. Soc.* **131**, 13943–13945 (2009).
20. Skrabalak, S. E. et al. Gold nanocages: Synthesis, properties, and applications. *Acc. Chem. Res.* **41**, 1587–1595 (2008).
21. Li, H. et al. Sequential cation exchange in nanocrystals: Preservation of crystal phase and formation of metastable phases. *Nano Lett.* **11**, 4964–4970 (2011).
22. Hong, S., Choi, Y. & Park, S. Shape control of Ag shell growth on Au nanodisks. *Chem. Mater.* **23**, 5375–5378 (2011).
23. Buck, M. R. & Schaak, R. E. Emerging strategies for the total synthesis of inorganic nanostructures. *Angew. Chem. Int. Ed.* **52**, 6154–6178 (2013).
24. Kalsin, A. M. et al. Electrostatic self-assembly of binary nanoparticle crystals with a diamond-like lattice. *Science* **312**, 420–424 (2006).
25. Kalsin, A. M., Kowalczyk, B., Smoukov, S. K., Klajn, R. & Grzybowski, B. A. Ionic-like behavior of oppositely charged nanoparticles. *J. Am. Chem. Soc.* **128**, 15046–15047 (2006).
26. Kalsin, A. M. & Grzybowski, B. A. Controlling the growth of "ionic" nanoparticle supracrystals. *Nano Lett.* **7**, 1018–1021 (2007).
27. Wang, L. Y., Albouy, P. A. & Pileni, M. P. Synthesis and self-assembly behavior of charged Au nanocrystals in aqueous solution. *Chem. Mater.* **27**, 4431–4440 (2015).
28. Kostiainen, M. A. et al. Electrostatic assembly of binary nanoparticle superlattices using protein cages. *Nat. Nanotech.* **8**, 52–56 (2013).
29. Liljeström, V., Seitsonen, J. & Kostiainen, M. A. Electrostatic self-assembly of soft matter nanoparticle cocrystals with tunable lattice parameters. *ACS Nano* **9**, 11278–11285 (2015).
30. Hassinen, J., Liljeström, V., Kostiainen, M. A. & Ras, R. H. A. Rapid cationization of gold nanoparticles by two-step phase transfer. *Angew. Chem. Int. Ed.* **54**, 7990–7993 (2015).
31. Laio, A. & Parrinello, M. Escaping free-energy minima. *Proc. Natl. Acad. Sci. U. S. A.* **99**, 12562–12566 (2002).
32. Barducci, A., Bussi, G. & Parrinello, M. Well-tempered metadynamics: A smoothly converging and tunable free-energy method. *Phys. Rev. Lett.* **100**, 020603 (2008).
33. Beyeh, N. K. et al. Crystalline cyclophane-protein cage frameworks. *ACS Nano* **12**, 8029–8036 (2018).
34. Schulze, H. Schwefelarsen in wässriger lösung. *J. Prakt. Chem.* **25**, 431–452 (1882).
35. Hardy, W. B. On the conditions which determine the stability of irreversible hydrosols. *Proc. R. Soc. London* **66**, 110–125 (1900).
36. Trefalt, G., Szilágyi, I. & Borkovec, M. Schulze-Hardy rule revisited. *Colloid Polym. Sci.* **298**, 961–967 (2020).
37. Gasparotto, P., Meißner, R. H. & Ceriotti, M. Recognizing local and global structural motifs at the atomic scale. *J. Chem. Theory Comput.* **14**, 486–498 (2018).
38. Bartók, A. P., Kondor, R. & Csányi, G. On representing chemical environments. *Phys. Rev. B* **87**, 184115 (2013).

39. Gasparotto, P., Bochicchio, D., Ceriotti, M. & Pavan, G. M. Identifying and tracking defects in dynamic supramolecular polymers. *J. Phys. Chem. B* **124**, 589–599 (2020).
40. Mackay, A. L. A dense non-crystallographic packing of equal spheres. *Acta Crystallogr.* **15**, 916–918 (1962).
41. Garzoni, M., Cheval, N., Fahmi, A., Danani, A. & Pavan, G. M. Ion-selective controlled assembly of dendrimer-based functional nanofibers and their ionic-competitive disassembly. *J. Am. Chem. Soc.* **134**, 3349–3357 (2012).
42. Astachov, V. et al. *In situ* functionalization of self-assembled dendrimer nanofibers with cadmium sulfide quantum dots through simple ionic-substitution. *New J. Chem.* **40**, 6325–6331 (2016).
43. Julin, S. et al. DNA origami directed 3D nanoparticle superlattice via electrostatic assembly. *Nanoscale* **11**, 4546–4551 (2019).
44. House, J. E. A TG study of the kinetics of decomposition of ammonium carbonate and ammonium bicarbonate. *Thermochim. Acta* **40**, 225–233 (1980).
45. Lofton, C. & Sigmund, W. Mechanisms controlling crystal habits of gold and silver colloids. *Adv. Funct. Mater.* **15**, 1197–1208 (2005).
46. Wang, D. et al. How and why nanoparticle's curvature regulates the apparent p*K*a of the coating ligands. *J. Am. Chem. Soc.* **133**, 2192–2197 (2011).
47. Boyer, P. D. Energy, life, and ATP (Nobel Lecture). *Angew. Chem. Int. Ed.* **37**, 2297–2307 (1998).
48. van Rossum, S. A. P., Tena-Solsona, M., van Esch, J. H., Eelkema, R. & Boekhoven, J. Dissipative out-of-equilibrium assembly of man-made supramolecular materials. *Chem. Soc. Rev.* **46**, 5519–5535 (2017).
49. Singh, N., Formon, G. J. M., De Piccoli, S. & Hermans, T. M. Devising synthetic reaction cycles for dissipative non-equilibrium self-assembly. *Adv. Mater.* **32**, 1906834 (2020).
50. Ragazzon, G. & Prins, L. J. Energy consumption in chemical fuel-driven self-assembly. *Nat. Nanotech.* **13**, 882–889 (2018).
51. Wang, G. & Liu, S. Strategies to construct a chemical-fuel-driven self-assembly. *ChemSystemsChem* **2**, e1900046 (2020).
52. Weißenfels, M., Gemen, J. & Klajn, R. Dissipative self-assembly: Fueling with chemicals versus light. *Chem* **7**, 23–37 (2021).
53. Grötsch, R. K. et al. Dissipative self-assembly of photoluminescent silicon nanocrystals. *Angew. Chem. Int. Ed.* **57**, 14608–14612 (2018).
54. Grötsch, R. K. et al. Pathway dependence in the fuel-driven dissipative self-assembly of nanoparticles. *J. Am. Chem. Soc.* **141**, 9872–9878 (2019).
55. van Ravensteijn, B. G. P., Hendriksen, W. E., Eelkema, R., van Esch, J. H. & Kegel, W. K. Fuel-mediated transient clustering of colloidal building blocks. *J. Am. Chem. Soc.* **139**, 9763–9766 (2017).
56. Hsu, C. C. et al. Role of synaptic vesicle proton gradient and protein phosphorylation on ATP-mediated activation of membrane-associated brain glutamate decarboxylase. *J. Biol. Chem.* **274**, 24366–24371 (1999).
57. Boekhoven, J. et al. Dissipative self-assembly of a molecular gelator by using a chemical fuel. *Angew. Chem. Int. Ed.* **49**, 4825–4828 (2010).
58. Leira-Iglesias, J., Sorrenti, A., Sato, A., Dunne, P. A. & Hermans, T. M. Supramolecular pathway selection of perylenediimides mediated by chemical fuels. *Chem. Commun.* **52**, 9009–9012 (2016).
59. Wang, G., Sun, J., An, L. & Liu, S. Fuel-driven dissipative self-assembly of a supra-amphiphile in batch reactor. *Biomacromolecules* **19**, 2542–2548 (2018).
60. Zhang, Y. X. & Zeng, H. C. Surfactant-mediated self-assembly of Au nanoparticles and their related conversion to complex mesoporous structures. *Langmuir* **24**, 3740–3746 (2008).

61. Klajn, R. et al. Bulk synthesis and surface patterning of nanoporous metals and alloys from supraspherical nanoparticle aggregates. *Adv. Funct. Mater.* **18**, 2763–2769 (2008).
62. Heo, K., Miesch, C., Emrick, T. & Hayward, R. C. Thermally reversible aggregation of gold nanoparticles in polymer nanocomposites through hydrogen bonding. *Nano Lett.* **13**, 5297–5302 (2013).
63. Stolzenburg, P., Hämisch, B., Richter, S., Huber, K. & Garnweitner, G. Secondary particle formation during the nonaqueous synthesis of metal oxide nanocrystals. *Langmuir* **34**, 12834–12844 (2018).
64. Reisler, E. & Egelman, E. H. Actin structure and function: What we still do not understand. *J. Biol. Chem.* **282**, 36133–36137 (2007).
65. Pfaendtner, J., Lyman, E., Pollard, T. D. & Voth, G. A. Structure and dynamics of the actin filament. *J. Mol. Biol.* **396**, 252–263 (2010).
66. Senesi, A. J. & Lee, B. Small-angle scattering of particle assemblies. *J. Appl. Crystallogr.* **48**, 1172–1182 (2015).

Acknowledgments. This work was supported by the European Research Council (ERC) (grants 820008 to R.K. and 818778 to G.M.P.), the Minerva Foundation with funding from the Federal German Ministry for Education and Research, and the Swiss National Science Foundation (grants 200021_175735 and IZLIZ2_183336 to G.M.P.). We acknowledge funding from the European Union's Horizon 2020 Research and Innovation Program under the Marie Skłodowska-Curie grant agreement no. 812868. Z.C. acknowledges support from the Planning and Budgeting Committee of the Council for Higher Education, the Koshland Foundation, and a McDonald–Leapman grant. The authors acknowledge the computational resources provided by the Swiss National Supercomputing Centre (CSCS). The support of the Irving and Cherna Moskowitz Center for Nano and Bio-Nano Imaging is gratefully acknowledged. This research used resources of the Advanced Photon Source, a U.S. Department of Energy (DOE) Office of Science User Facility, operated for the DOE Office of Science by Argonne National Laboratory under Contract No. DE-AC02-06CH11357. Extraordinary facility operations were supported in part by the DOE Office of Science through the National Virtual Biotechnology Laboratory, a consortium of DOE national laboratories focused on the response to COVID-19, with funding provided by the Coronavirus CARES Act.

Author contributions. T.B. synthesized positively charged nanoparticles, studied their interactions with oligoanions, and developed a method to prepare crystalline nanoparticle aggregates. A.G. and C.P. performed the computational studies. J.G. developed the reverse system of negatively charged nanoparticles and oligocations. B.L. performed and analyzed SAXS measurements. N.E. and L.H. performed cryo-STEM imaging and analysis. Z.C. contributed to the characterization of nanoparticles. R.K. supervised the project, coordinated with G.M.P. on computational studies, and prepared the manuscript, with contributions from all authors.

Competing interests. The authors declare no competing interests.

Figure captions

Fig. 1 | Electrostatic co-assembly between positively charged nanoparticles and negatively charged small molecules. a, Typical aggregation behavior of oppositely charged species on a molecular scale (left) and a nanoscale (right). **b,** Structural formula of (11-mercaptoundecyl)-*N*,*N*,*N*-

trimethylammonium (TMA) used for stabilizing gold nanoparticles (NPs) in water (counterion, Br^-); *right:* a representative TEM image of TMA-functionalized 7.4 nm Au NPs (Au·TMA). **c,** Examples of multiply charged anions capable of mediating attractive interactions between Au·TMA. **d,** Representative titration curve for the titration of Au·TMA (here, 11.4 nm; overall 20 nmol of TMA groups) with EDTA trisodium salt. The dashed red line denotes the point of electroneutrality (~6.7 nmol of trianionic $EDTA^{3-}$). **e,** Representative titration curve for the titration of EDTA (trisodium salt) (6 nmol), with 11.4 nm Au·TMA. The dashed red line denotes the point of electroneutrality (18 nmol TMA on Au NPs).

Fig. 2 | Molecular dynamics simulations of electrostatic interactions between positively charged nanoparticles and small anions. a, Atomistic model of one-half of a TMA-functionalized Au NP (here, interacting with citrate) used in the all-atom simulations. **b,** Free-energy profile for the interaction between Au·TMA and Cl^- (yellow), HPO_4^{2-} (blue) or $citrate^{3-}$ (red) (expressed as a function of the distance *d* between the center of mass of the anion and the center of mass of the closest TMA charged headgroup; errors bars are calculated as the standard error of the mean). **c,** Snapshots from CG-MD simulations of two TMA-coated Au NPs in the presence of HPO_4^{2-} (top) or $citrate^{3-}$ (bottom). **d,** Distance between the centers of two TMA-functionalized Au NPs in the presence of HPO_4^{2-} (blue) or $citrate^{3-}$ (red) as a function of the CG-MD simulation time.

Fig. 3 | Dynamics of small anions and the annealing of TMA-functionalized Au NPs. a, Snapshots from a CG-MD simulation of two Au·TMA NPs in the presence of citrate ions after stable binding of the two NPs (0.9 μs), and at the end of the CG-MD simulation (8.4 μs). Red, green, and gray identify citrates grouped into three different macro-clusters at t = 0.9 μs (the NPs are represented as solid yellow spheres, with TMA ligands omitted for clarity). **b,** A two-dimensional free-energy surface associated with the configurations of citrate ions as a function of two variables, *CONT* and *DIST* (for definitions, see Supporting Information, Section 4.2.2). The areas encircled by dashed-line ovals denote three local energy minima corresponding to citrates interacting with a single NP (gray), located at the interface between the two NPs (red), and an intermediate state (green). The black arrows denote transitions between the three states, with the numbers next to the arrows indicating the relative probability of a given transition. **c,** Annealing of Au·TMA/citrate aggregates at 23 ºC over 24 h. **d,** Annealing of Au·TMA/citrate aggregates at 50 ºC over 24 h. **e,** Representative cryo-STEM bright-field image of an Au·TMA/$P_3O_{10}^{5-}$ aggregate. The entity inside the turquoise square is a NP_{55} Mackay cluster. **f,** *Top:* Voxel projections of the tomographic reconstruction of the cluster marked in (e). The three projections shown correspond to the 5-fold, 3-fold, and 2-fold symmetry. *Bottom:* Matching projections of a model Mackay cluster. Scale bars in the insets, 50 nm.

Fig. 4 | Self-assembly of co-crystals of TMA-functionalized Au NPs and small anions. a, Schematic illustration of the method for anion-mediated crystallization of Au·TMA (the counterion for multiply charged anions, indicated in green, is Na^+. Ammonium ions and ammonia are shown in red; carbonate ions and carbon dioxide are shown in blue). **b-h,** Representative SEM images of colloidal crystals of Au·TMA and various multiply charged anions: $P_3O_{10}^{5-}$ (**b, e, g, h**), $EDTA^{3-}$ (**f**), $citrate^{3-}$ (**d**), and ATP^{4-} (**c**). The size of Au NPs was 7.4 nm (**b, c, e**), 11.4 nm (**d, f**), and 4.7 nm (**g, h**). For additional images, see Extended Data Fig. 1. **i,** Optical micrograph of colloidal crystals of 4.7 nm Au·TMA and $P_3O_{10}^{5-}$. **j,** 1D X-ray diffraction (SAXS) patterns for 4.73 nm Au·TMA/ $P_3O_{10}^{5-}$ crystals. SAXS data are plots of scattered intensity I(q) (y-axis, arbitrary units) vs. scattering vector q (x-axis, $Å^{-1}$). Black traces are experimental data; pink and blue traces are modeled SAXS patterns for perfect lattices (pink: a = 121.3 Å; blue: a = 130.9 Å). **k,** Proposed models of binding within crystals with a smaller (top; major species) and larger (bottom; minor species) lattice constants. **l,** 1D SAXS patterns for 4.73 nm Au·TMA/ATP crystals. Black traces are experimental data; pink and blue traces are modeled SAXS patterns for perfect lattices (pink: a = 119.8 Å; blue: a = 130.9 Å).

Fig. 5 | Electrostatic co-assembly of negatively charged nanoparticles and positively charged small molecules. a, Structural formula of 11-mercaptoundecanesulfonate (MUS) used for stabilizing gold NPs in water (counterion, Na^+); *right:* a representative TEM image of MUS-functionalized 4.7 nm Au NPs. **b,** Structural formulas of an organic trication capable of mediating attractive interactions between Au·MUS (octamethyldiethylenetriammonium; OMA^{3+}) and a control dication (hexamethylethanediammonium; HMA^{2+}) (counterions, I^-). **c,** Solid markers: a representative titration curve for the titration of Au·MUS (4.7 nm; overall 50 nmol of MUS groups) with OMA^{3+}. The dashed red line denotes the point of electroneutrality (~16.7 nmol of OMA^{3+}). Empty markers: control titration with HMA^{2+}. **d,** Solid markers: a representative titration curve for the titration of OMA^{3+} (20 nmol) with 4.7 nm Au·MUS. The dashed red line denotes the point of electroneutrality (60 nmol MUS on Au NPs). Empty markers: a control titration with of HMA^{2+} with the same NPs. **e-f,** Representative SEM images of colloidal crystals of Au·MUS and OMA^{3+}.

Fig. 6 | Dissipative self-assembly of gold nanoparticles driven by ATP. a, Structural formulas of ATP and inorganic triphosphate. **b,** Schematic representation of the ATP-induced dissipative self-assembly (DSA) of Au·TMA. The assembly/disassembly cycle is associated with an exergonic reaction of the hydrolysis of ATP into AMP and HPO_4^{2-}. **c,** A series of UV/Vis absorption spectra of TMA-functionalized 7.4 nm Au NPs (n_{TMA} = 19.2 nmol) in the presence of 11.1 units/mL of apyrase before and after injecting a solution of ATP (n_{ATP} = 54 nmol). **d,** Changes in the maxima of the dynamic light scattering (DLS) profiles of a solution of the same Au·TMA (with 11.1 units/mL of apyrase) after injecting 40.5 nmol of ATP at t = 0. **e,** Representative SEM images of 7.4 nm Au·TMA (11.1 units/mL of apyrase) before (t = 0) and after different time intervals following the injection of 54 nmol of ATP. **f,** Six cycles of DSA of Au·TMA in the presence of 1000 units/mL of alkaline phosphatase (ALPase), followed by monitoring the position of the NPs' SPR band. For each cycle, 54 nmol of ATP was used. **g,** Six cycles of DSA of Au·TMA (1000 units/mL of ALPase), followed by monitoring the absorbance at 800 nm. Each cycle was initiated by injecting 54 nmol of ATP. **h,** Stimulus-dependent disassembly profiles of aggregates of Au·TMA in the presence of ALPase (200 units/mL). Solid triangles denote ATP (12 nmol); empty circles denote inorganic triphosphate (9 nmol). **i,** Representative cryo-TEM image of 4.7 nm Au·TMA/ $P_3O_{10}^{5-}$ aggregates. **j,** Representative cryo-TEM image of 4.7 nm Au·TMA/ATP aggregates (the scale bar in the inset corresponds to 20 nm). **k,** Controlling the lifetimes of dynamic NP aggregates by the amount of added ATP injected at t = 0 (in all cases, 200 units/mL of ALPase were used). **l,** Controlling the lifetimes of dynamic NP aggregates by the amount of a phosphatase enzyme (here, apyrase; in all cases, 54 nmol of ATP were injected at t = 0). In panels b–d and h, the syringe indicates injection of an oligophosphate stimulus and the petrol pump indicates the availability of the stimulus.

Methods

General information. All chemicals were of analytical grade and were used as received. Scanning electron microscopy (SEM) was carried out on a Zeiss Ultra 55 microscope (operating at 10 kV unless indicated otherwise). Transmission electron microscopy (TEM) was carried out on a JEOL JEM-2100 microscope (operating at 200 kV). UV/Vis absorption spectra were recorded on a Shimadzu UV-2700 spectrophotometer. ^{1}H NMR spectra were recorded on a Bruker Avance III 400 MHz NMR spectrometer (30 scans; relaxation delay of 20 s). Dynamic light scattering (DLS) measurements were performed on a Zetasizer Nano ZS (Malvern). SAXS measurements were carried out at the 12-ID-B beamline of the Advanced Photon Source (APS), Argonne National Laboratory. Aqueous suspensions of crystalline NP aggregates were placed inside quartz capillaries. Each sample was exposed to X-ray beams with energy of 14 keV for 1 s. Scattered photons were counted with a Pilatus2M detector located about 2 m downstream of the sample. Collected 2D SAXS images were azimuthally averaged with the software provided at the beamline. The diffraction patterns were simulated as reported elsewhere[66,67]. For the simulation, particle sizes were determined from solution SAXS measurements. The diffraction patterns were indexed by a custom-built software and the space groups were determined to yield the highest

symmetry, assuming perfect spherical particles. The Debye–Waller factor and micro-strain used for the simulation were about 2.5% and 1.0%, respectively. The domain size was approximated to about 500 nm.

Molecular dynamics simulations. TMA-functionalized Au NPs and anions (citrate and hydrogen phosphate HPO_4^{2-}) were built and simulated at two different molecular resolutions: all-atom (AA) and coarse-grained (CG), where the resolution in the CG models is ~5 Å (Supplementary Fig. 7). All the AA and CG simulations were conducted using GROMACS 2018.6 software[68] patched with the PLUMED 2 plugin[69]. Further details are provided in Supporting Information, Section 5.

Preparation of crystalline assemblies of positively charged nanoparticles and small anions. Supracrystals of TMA-functionalized Au NPs (Au·TMA) and multiply charged anions (Supplementary Fig. 4) were prepared by slowly decreasing the ionic strength of the solution by the spontaneous decomposition of $(NH_4)_2CO_3$ (see the scheme in Fig. 4a). In a typical experiment, Au·TMA dissolved in water was treated with an aqueous solution of a multiply charged anion under vigorous shaking until the NPs' λ_{SPR} plateaued (see Fig. 1d, Supplementary Fig. 5a). The resulting aggregates were collected by centrifugation, washed twice with deionized water, and dispersed in a small volume (typically 200 μL) of a 2.5 M aqueous solution of $(NH_4)_2CO_3$, resulting in a solution of well dispersed NPs. The sample was left for 24 h, resulting in the quantitative precipitation of the NPs in the form of colloidal crystals. Representative SEM images of Au·TMA co-crystallized with different multiply charged anions are shown in Fig. 4b–h and Extended Data Fig. 2.

Preparation of crystalline assemblies of negatively charged nanoparticles and small cations. Supracrystals of MUS-functionalized Au NPs (Au·MUS) and trications (Supplementary Fig. 20) were prepared by slowly decreasing the ionic strength of the solution by the spontaneous decomposition of $(NH_4)_2CO_3$ (see the scheme in Fig. 4a). In a typical experiment, Au·MUS dissolved in water was treated with an aqueous solution of OMA^{3+} under vigorous shaking until the NPs' λ_{SPR} plateaued (see Fig. 5c). The resulting aggregates were collected by centrifugation, washed twice with deionized water, and dispersed in a small volume (typically 200 μL) of a 0.5 M aqueous solution of $(NH_4)_2CO_3$, resulting in a solution of well dispersed NPs. The sample was left for 24 h, resulting in the quantitative precipitation of the NPs in the form of colloidal crystals. Representative SEM images of Au·MUS co-crystallized with OMA^{3+} are shown in Fig. 5e-f and Extended Data Fig. 4.

Cryo-TEM analysis of aggregates of charged nanoparticles and oppositely charged small ions. Aggregates of 4.7 nm Au·TMA and $P_3O_{10}^{5-}$ and aggregates of 4.7 nm Au·TMA and ATP were first prepared by mixing 64 nmol Au·TMA (in terms of surface TMA ligands) in 100 μL of water with 12.8 nmol of $P_3O_{10}^{5-}$ and 16 nmol of ATP, both dissolved in 5 μL of water. Immediately thereafter, TEM specimens were prepared by transferring 2.5 μL of aqueous suspensions of the NP aggregates onto glow-discharged Quantifoil Cu 300-mesh R 2/1 or R 3.5/1 holey carbon grids, blotted for 3 seconds at 100% humidity, and plunge frozen in liquid ethane cooled by liquid nitrogen using a Vitrobot plunger (Thermo Fisher Scientific). The grids were loaded onto a Talos Arctica electron microscope (Thermo Fisher Scientific) and imaged under liquid nitrogen temperature. Cryo-TEM and cryo-STEM images were taken under low-dose conditions at an acceleration voltage of 200 kV. TEM images were recorded with a Gatan OneView camera (Gatan, Inc.), STEM images were collected with a bottom-mount bright-field detector (Thermo Fisher Scientific). Cryo-STEM tomograms (CSTET) were collected by tilting the sample along a single axis, spanning a tilt range from up to –60° to 60° with a tilt increment of 2°. 2k×2k scan frames were recorded with a probe semi-convergence angle of 1.3 mrad, a beam current of approximately 10 pA, a sampling rate of 0.60 nm per pixel, and a dwell time of 5 μs per pixel, resulting in an exposure of approximately 9 electrons per $Å^2$ per frame. These settings were kept constant for all tomograms. Tomograms were reconstructed using the iterative simultaneous reconstruction technique. In order to avoid air–water interface artefacts, we analyzed only those structures that were located in the bulk of the cryo-STEM tomography samples that had thicknesses of 200-400 nm. The three-dimensional reconstruction was done after cross-correlation alignment and displacement refinement using an iterative feedback loop algorithm as described before[70]. Quantitative order analysis was based on computational procedures described in detail in a previous publication[71].

References

67. Macfarlane, R. J. et al. Nanoparticle superlattice engineering with DNA. *Science* **334**, 204–208 (2011).
68. Abraham, M. J. et al. GROMACS: High performance molecular simulations through multi-level parallelism from laptops to supercomputers. *SoftwareX (Netherlands)* **1–2**, 19–25 (2015).
69. Tribello, G. A., Bonomi, M., Branduardi, D., Camilloni, C. & Bussi, G. PLUMED 2: New feathers for an old bird. *Comput. Phys. Commun.* **185**, 604–613 (2014).

70. Houben, L. & Bar Sadan, M. Refinement procedure for the image alignment in high-resolution electron tomography. *Ultramicroscopy* **111**, 1512–1520 (2011).
71. Houben, L., Weissman, H., Wolf, S. G. & Rybtchinski, B. A mechanism of ferritin crystallization revealed by cryo-STEM tomography. *Nature* **579**, 540–543 (2020).

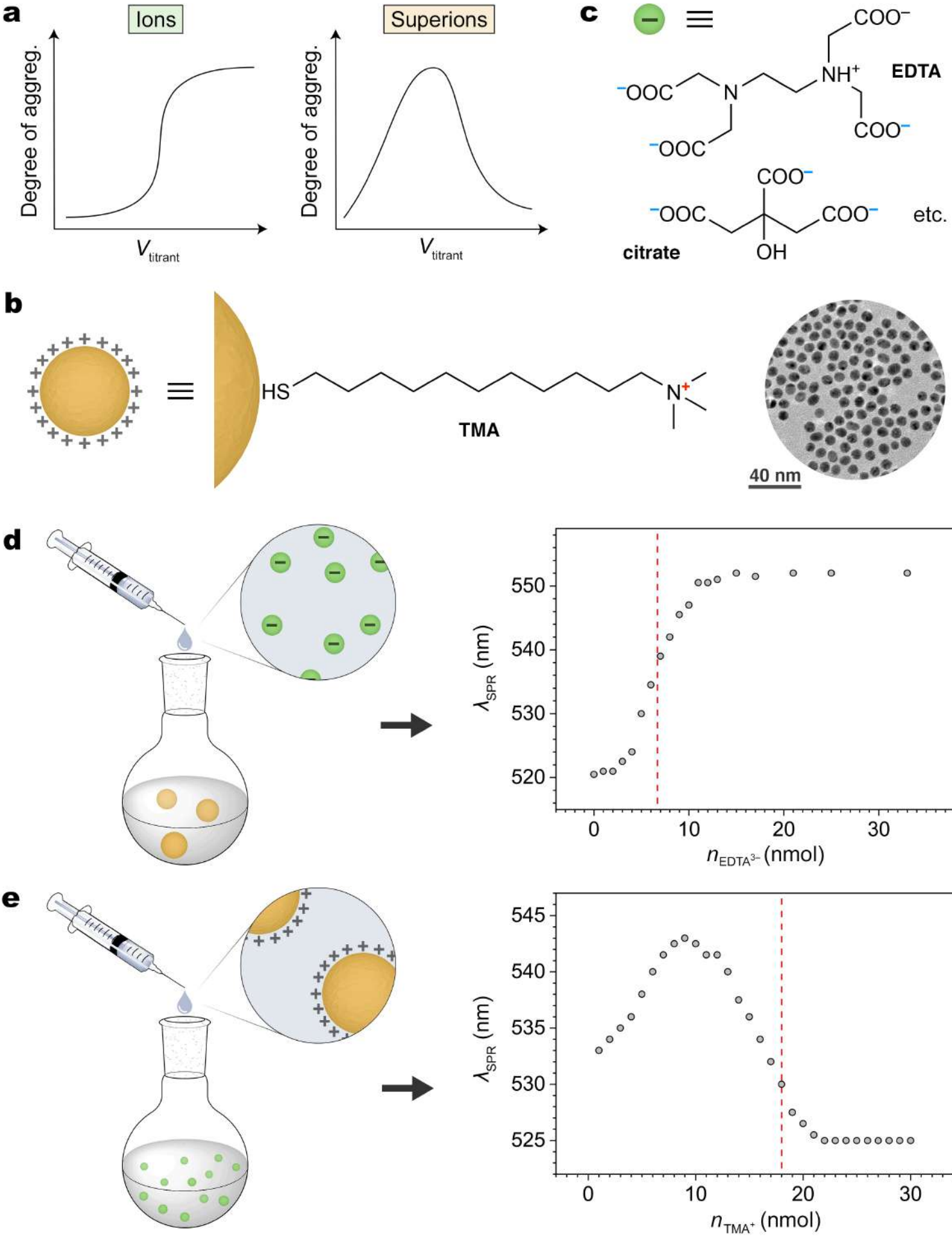
a
Ions
Superions
Degree of aggreg.
$V_{titrant}$
c
EDTA
citrate
etc.
b
HS
TMA
40 nm
d
λ_{SPR} (nm)
$n_{EDTA^{3-}}$ (nmol)
e
$n_{TMA^{+}}$ (nmol)

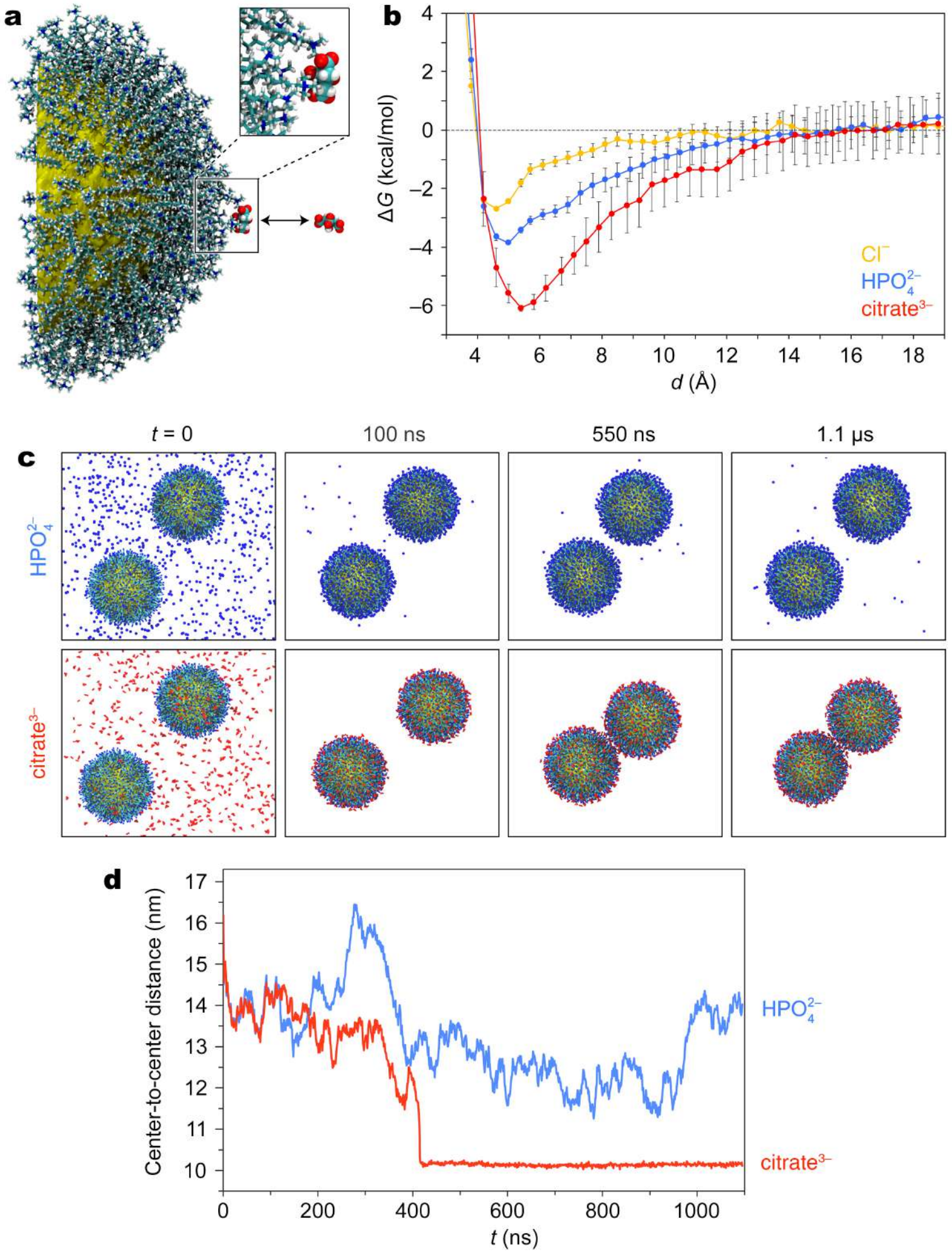
a
b
ΔG (kcal/mol)
d (Å)
Cl⁻
HPO4 2–
citrate3–
c
t = 0
100 ns
550 ns
1.1 μs
HPO4 2–
citrate3–
d
Center-to-center distance (nm)
t (ns)
HPO4 2–
citrate3–

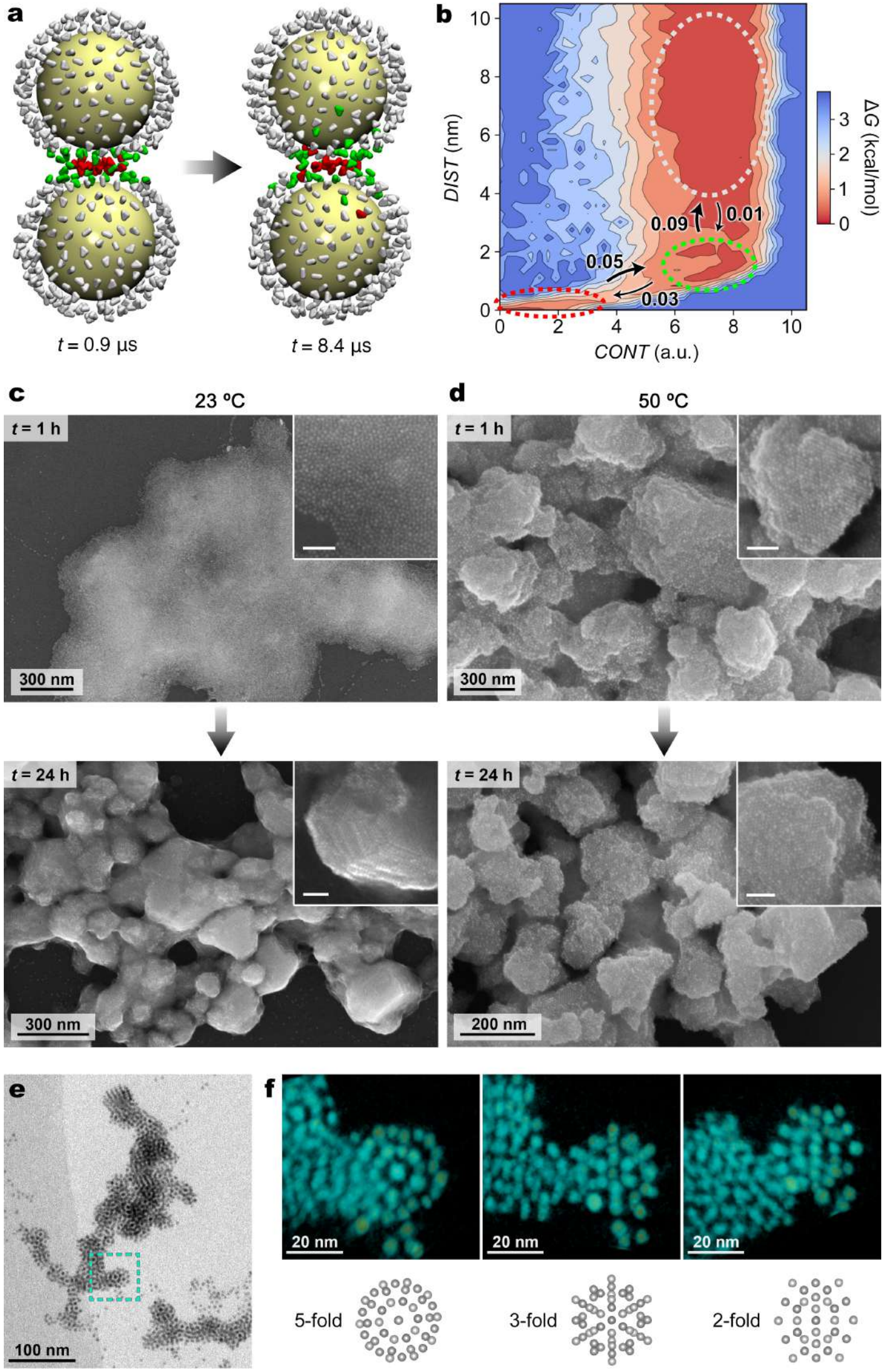
a
t = 0.9 μs
t = 8.4 μs
b
DIST (nm)
CONT (a.u.)
ΔG (kcal/mol)
0.09
0.01
0.05
0.03
c
23 °C
t = 1 h
300 nm
t = 24 h
300 nm
d
50 °C
t = 1 h
300 nm
t = 24 h
200 nm
e
100 nm
f
20 nm
20 nm
20 nm
5-fold
3-fold
2-fold

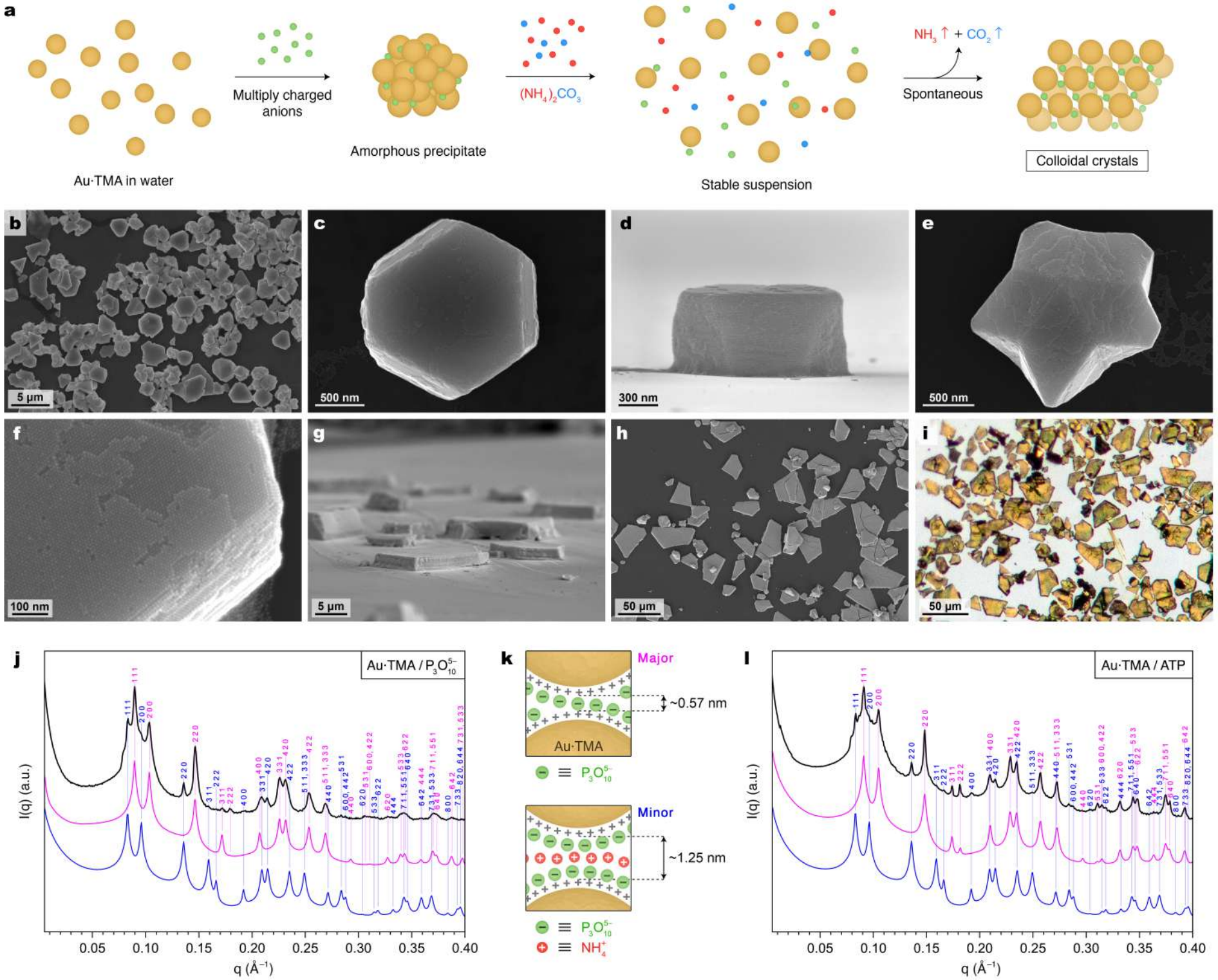
a
Au·TMA in water
Multiply charged anions
Amorphous precipitate
(NH4)2CO3
Stable suspension
NH3 ↑ + CO2 ↑
Spontaneous
Colloidal crystals
b
5 μm
c
500 nm
d
300 nm
e
500 nm
f
100 nm
g
5 μm
h
50 μm
i
50 μm
j
Au·TMA / P3O10 5−
I(q) (a.u.)
q (Å−1)
k
Major
~0.57 nm
Au·TMA
≡ P3O10 5−
Minor
~1.25 nm
≡ P3O10 5−
≡ NH4+
l
Au·TMA / ATP
I(q) (a.u.)
q (Å−1)

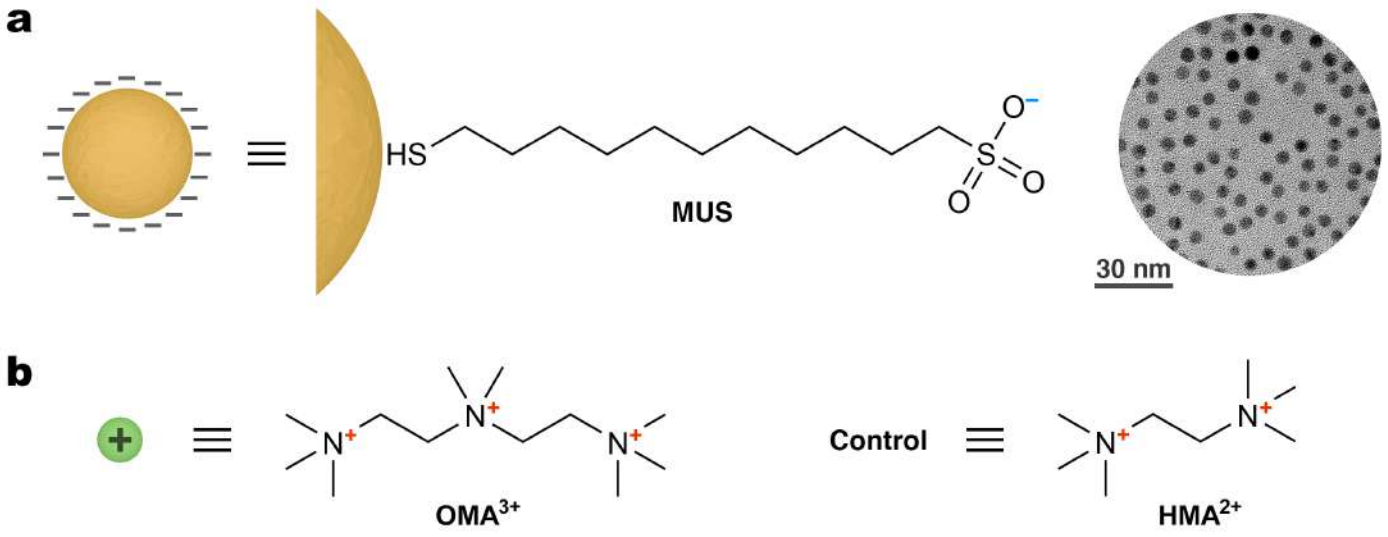
a
HS
MUS
30 nm
b
OMA3+
Control
HMA2+
c
OMA3+
HMA2+
λSPR (nm)
nOMA3+/HMA2+ (nmol)
d
OMA3+
HMA2+
λSPR (nm)
nMUS− (nmol)
e
20 μm
f
5 μm

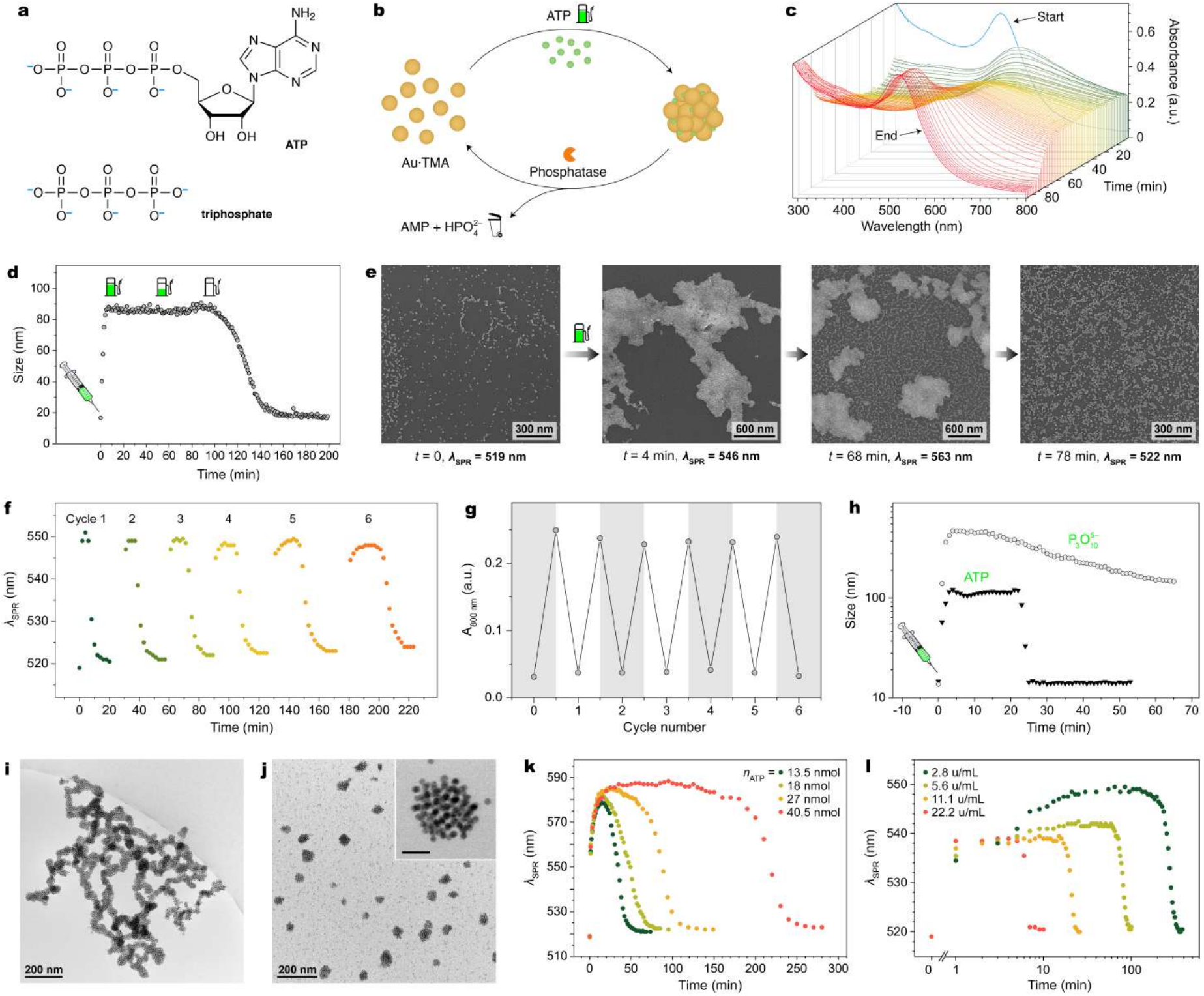
a
ATP
triphosphate
b
ATP
Au·TMA
Phosphatase
AMP + HPO4 2−
c
Start
End
Absorbance (a.u.)
Time (min)
Wavelength (nm)
d
Size (nm)
Time (min)
e
300 nm
600 nm
600 nm
300 nm
t = 0, λSPR = 519 nm
t = 4 min, λSPR = 546 nm
t = 68 min, λSPR = 563 nm
t = 78 min, λSPR = 522 nm
f
Cycle 1
2
3
4
5
6
λSPR (nm)
Time (min)
g
A600 nm (a.u.)
Cycle number
h
P3O10 5−
ATP
Size (nm)
Time (min)
i
200 nm
j
200 nm
k
nATP =
13.5 nmol
18 nmol
27 nmol
40.5 nmol
λSPR (nm)
Time (min)
l
2.8 u/mL
5.6 u/mL
11.1 u/mL
22.2 u/mL
λSPR (nm)
Time (min)

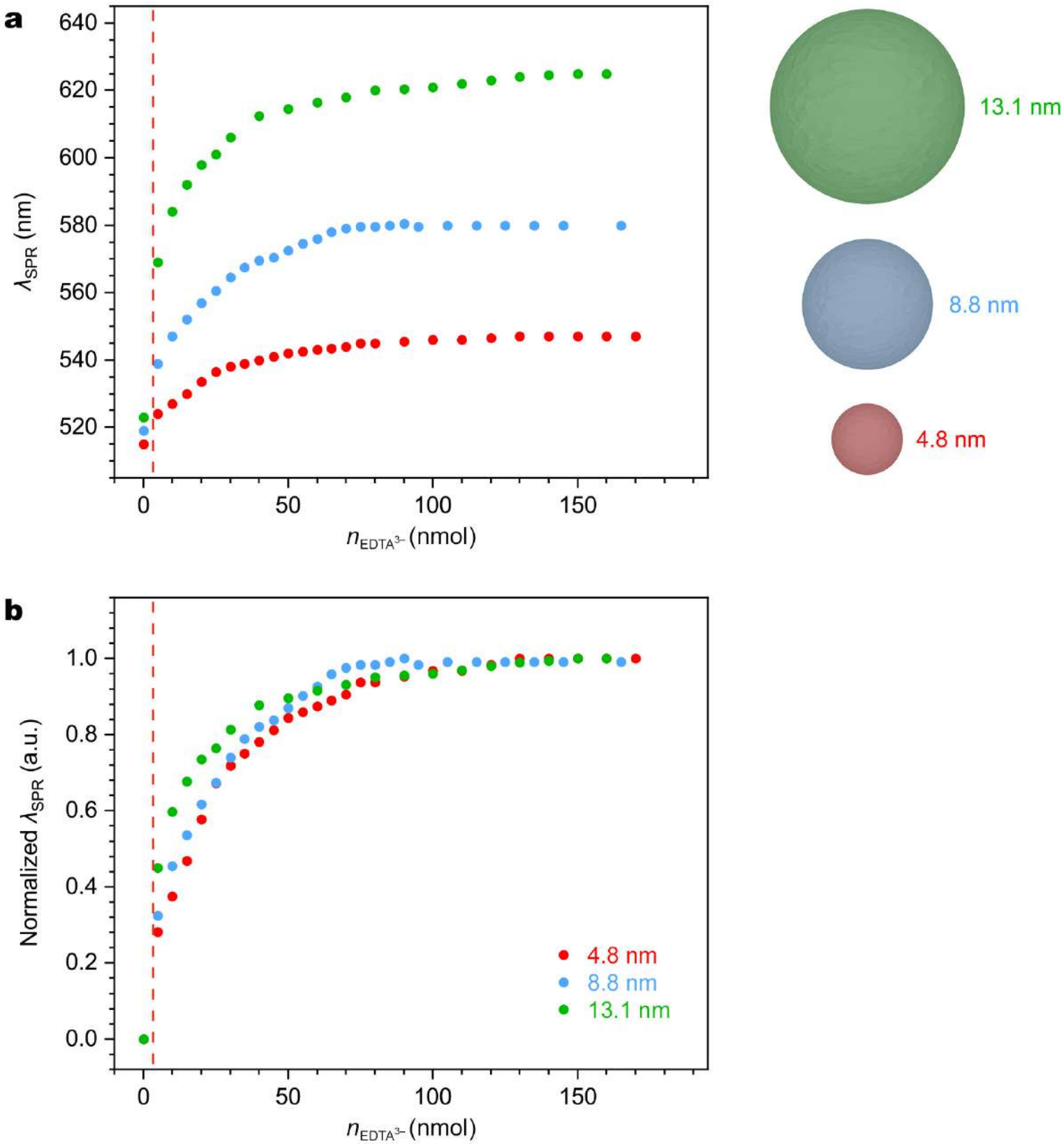
a
640
620
600
580
560
540
520
λ_{SPR} (nm)
0
50
100
150
$n_{EDTA^{3-}}$ (nmol)
13.1 nm
8.8 nm
4.8 nm
b
1.0
0.8
0.6
0.4
0.2
0.0
Normalized λ_{SPR} (a.u.)
0
50
100
150
$n_{EDTA^{3-}}$ (nmol)
4.8 nm
8.8 nm
13.1 nm

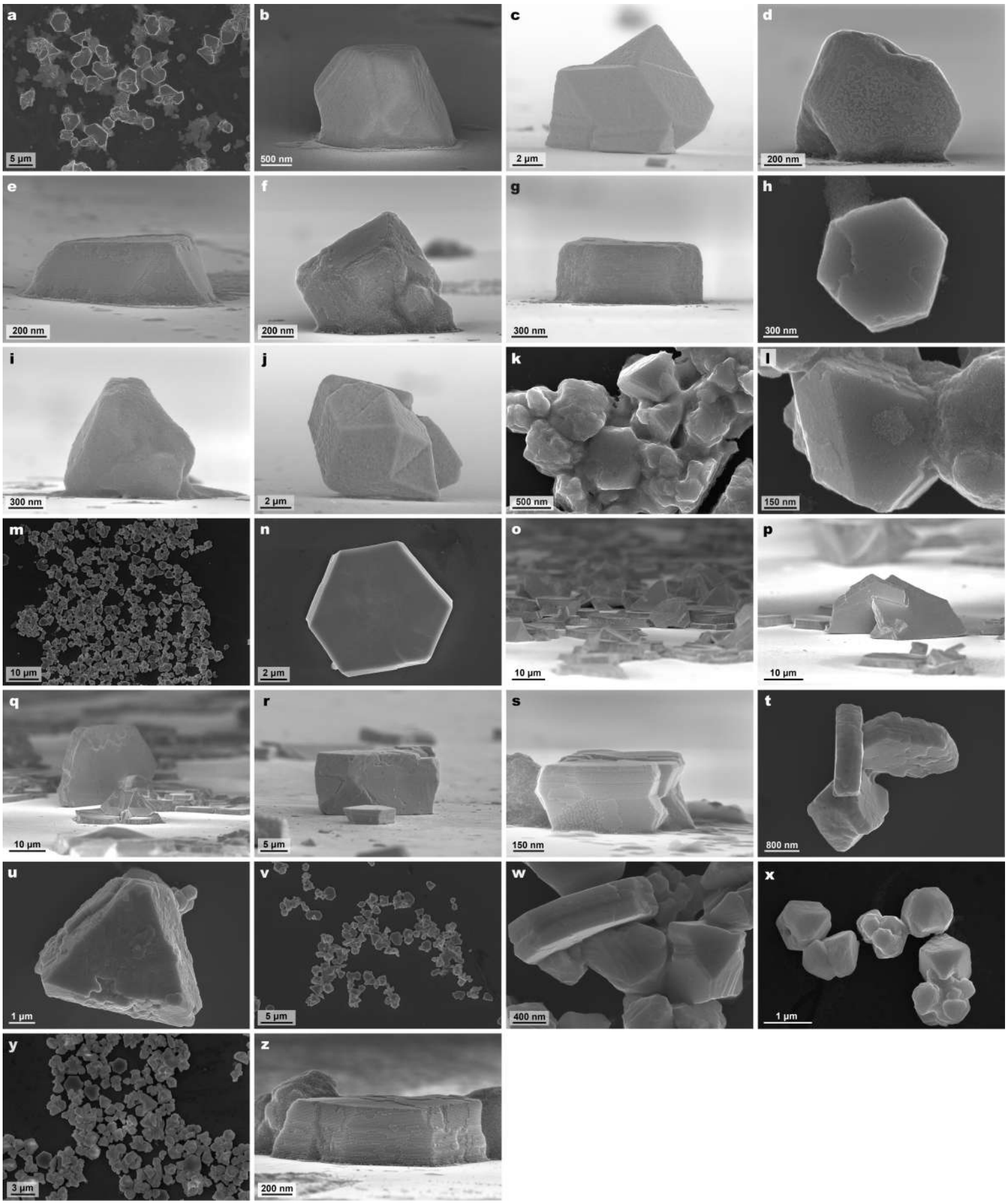
a
5 µm
b
500 nm
c
2 µm
d
200 nm
e
200 nm
f
200 nm
g
300 nm
h
300 nm
i
300 nm
j
2 µm
k
500 nm
l
150 nm
m
10 µm
n
2 µm
o
10 µm
p
10 µm
q
10 µm
r
5 µm
s
150 nm
t
800 nm
u
1 µm
v
5 µm
w
400 nm
x
1 µm
y
3 µm
z
200 nm

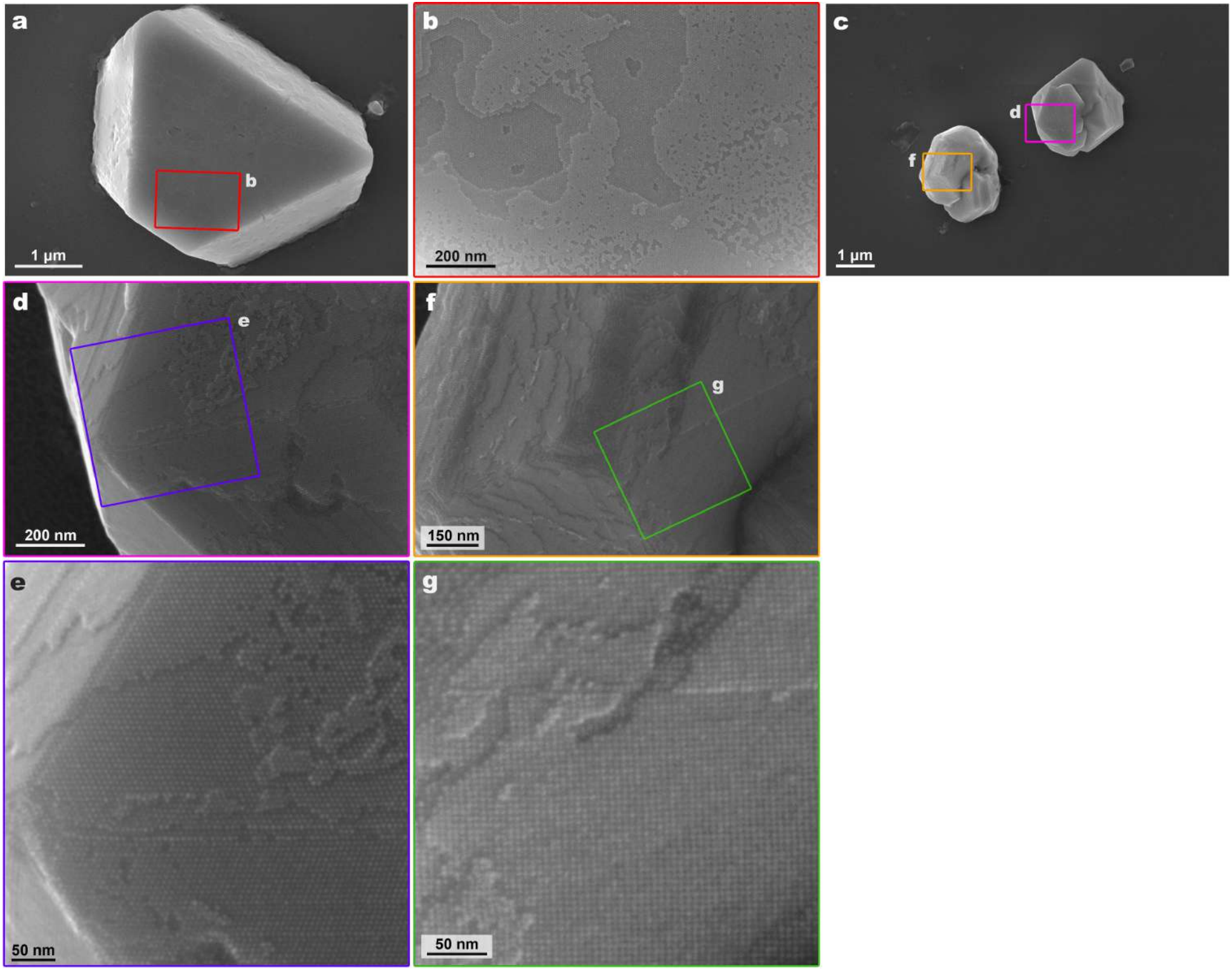
a
b
1 μm
b
200 nm
c
d
f
1 μm
d
e
200 nm
f
g
150 nm
e
50 nm
g
50 nm

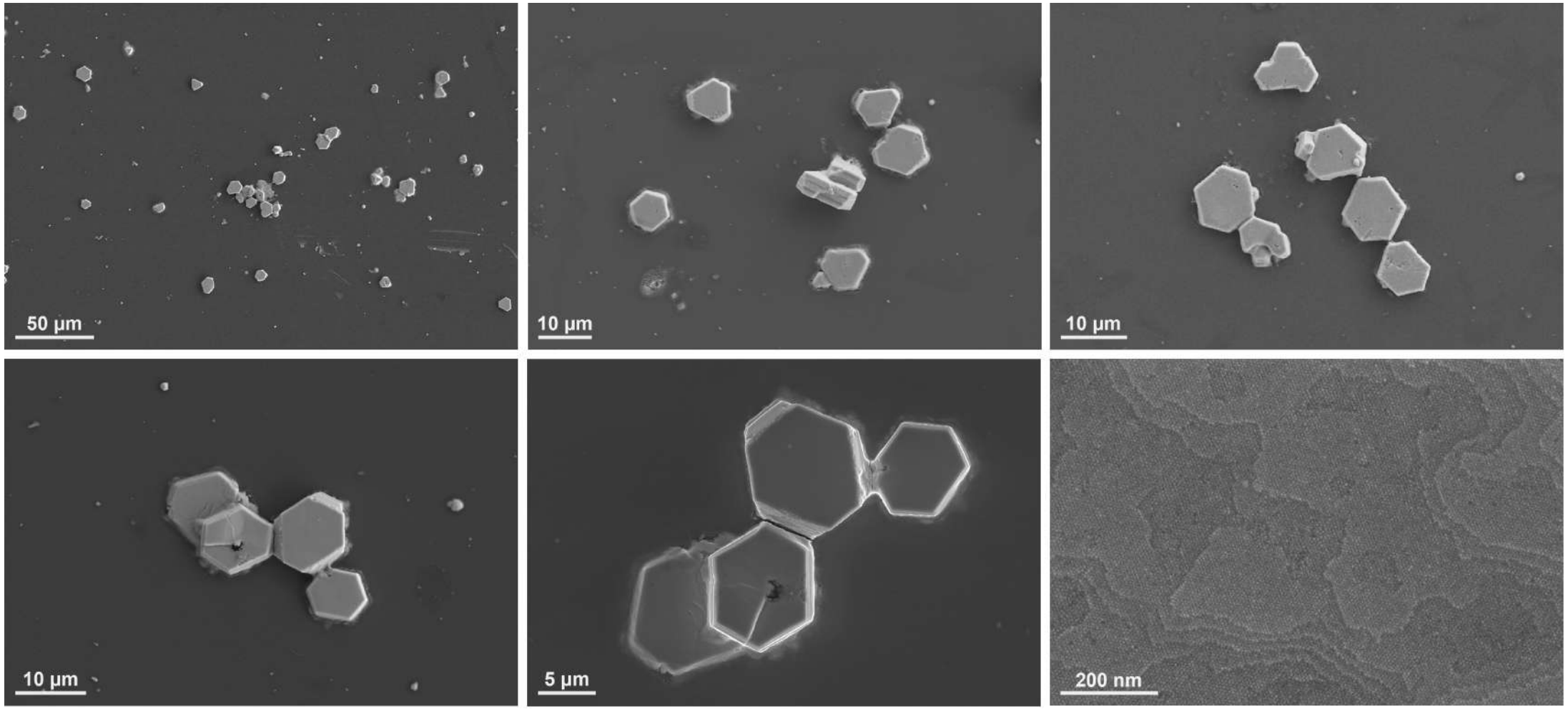
50 µm
10 µm
10 µm
10 µm
5 µm
200 nm

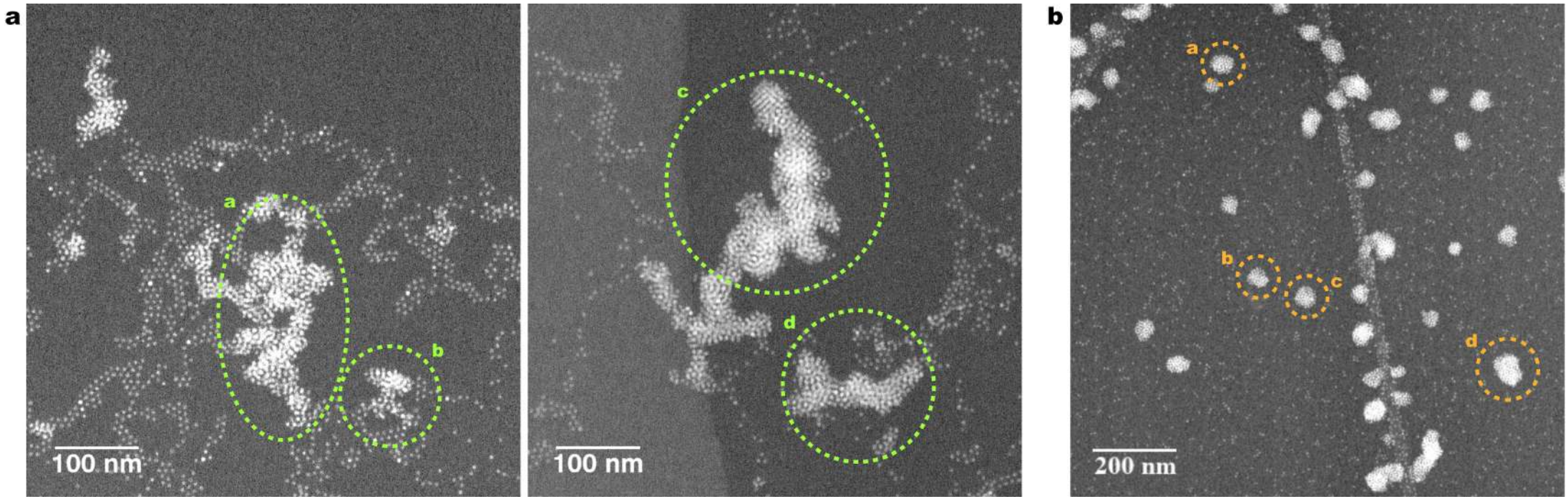
a
a
b
100 nm
c
d
100 nm
b
a
b
c
d
200 nm

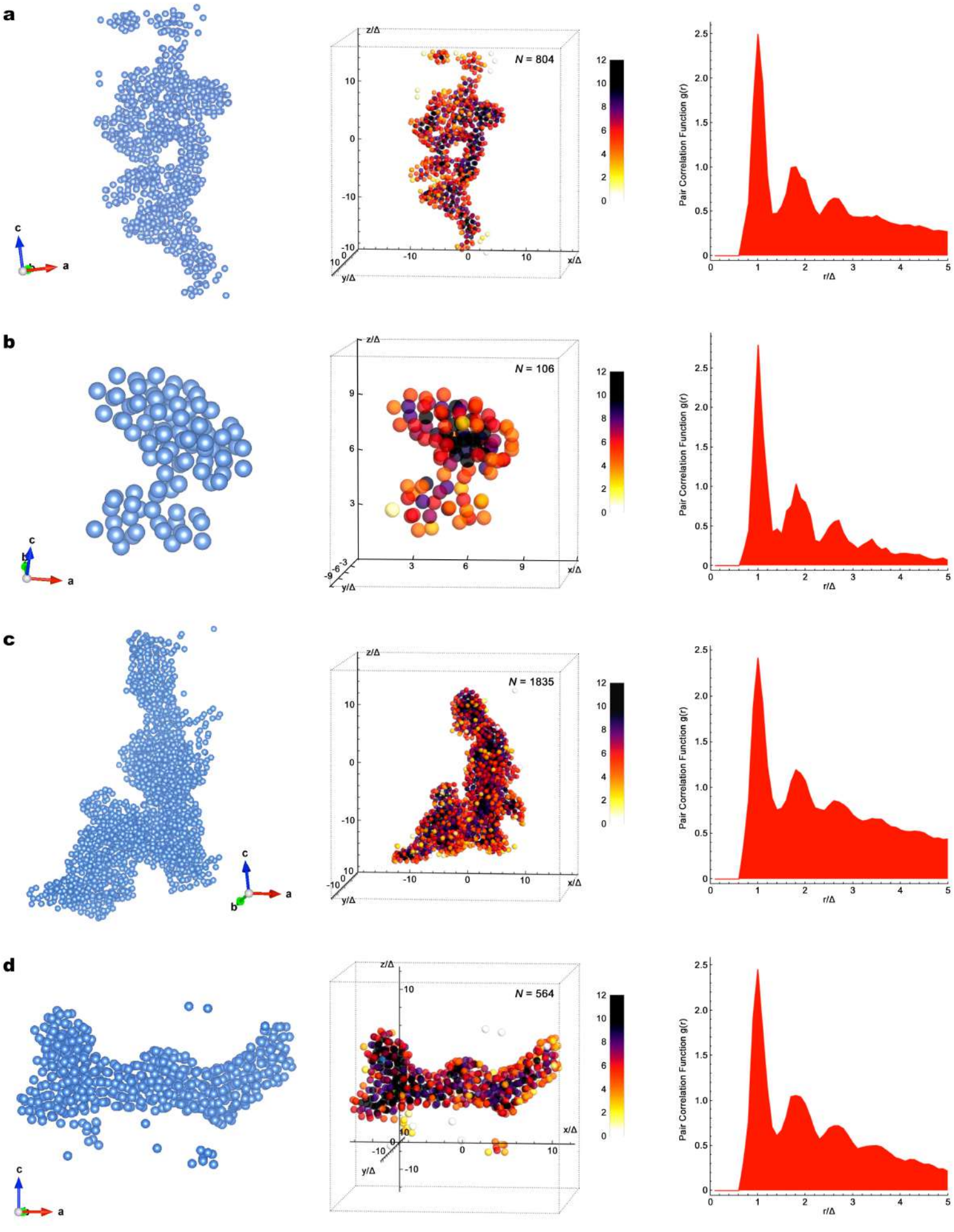
a
c
a
z/Δ
N = 804
x/Δ
y/Δ
Pair Correlation Function g(r)
r/Δ
b
c
b
a
z/Δ
N = 106
x/Δ
y/Δ
Pair Correlation Function g(r)
r/Δ
c
c
b
a
z/Δ
N = 1835
x/Δ
y/Δ
Pair Correlation Function g(r)
r/Δ
d
c
a
z/Δ
N = 564
x/Δ
y/Δ
Pair Correlation Function g(r)
r/Δ

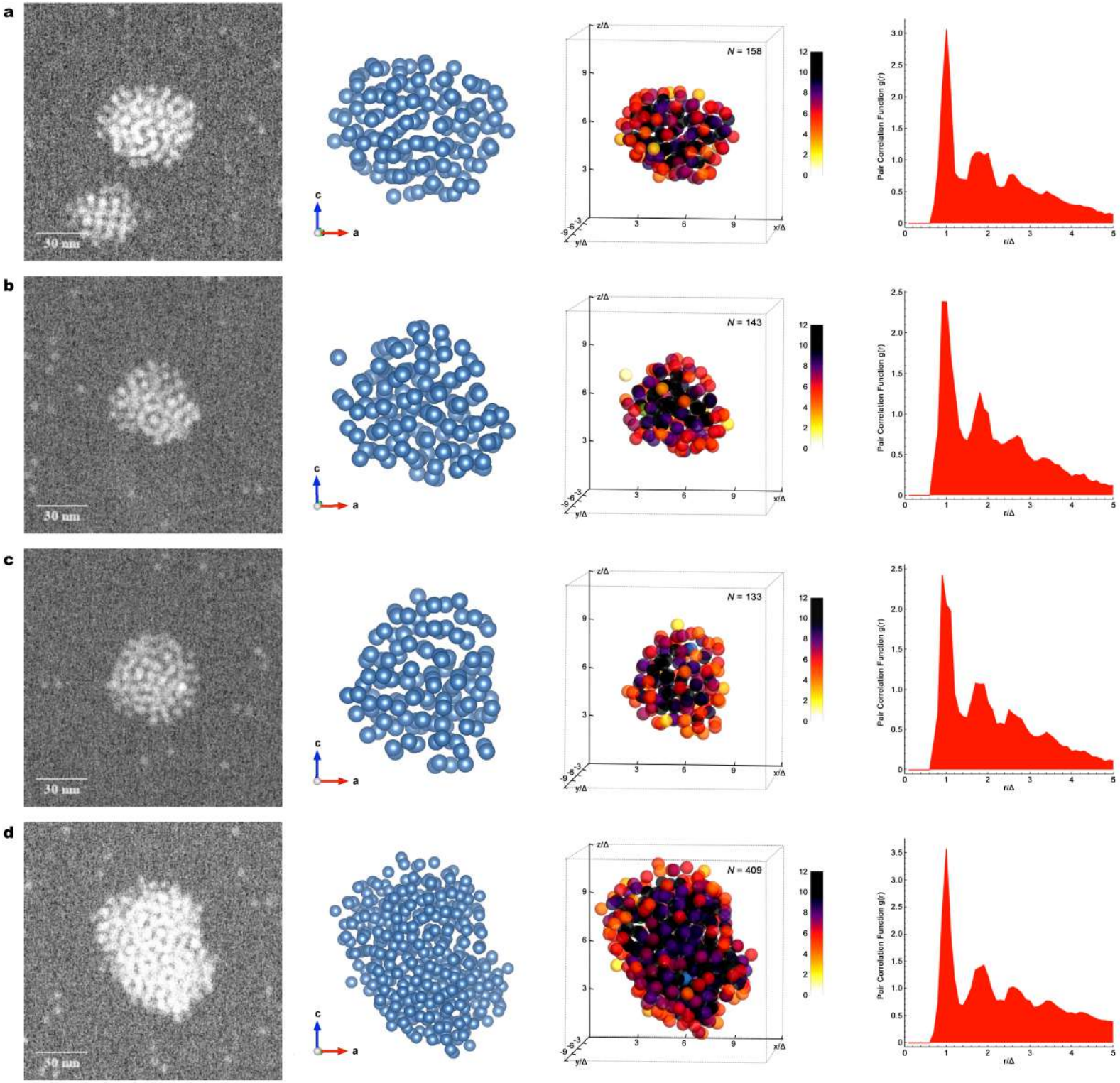
a
b
c
d
30 nm
c
a
z/Δ
x/Δ
y/Δ
N = 158
N = 143
N = 133
N = 409
Pair Correlation Function g(r)
r/Δ

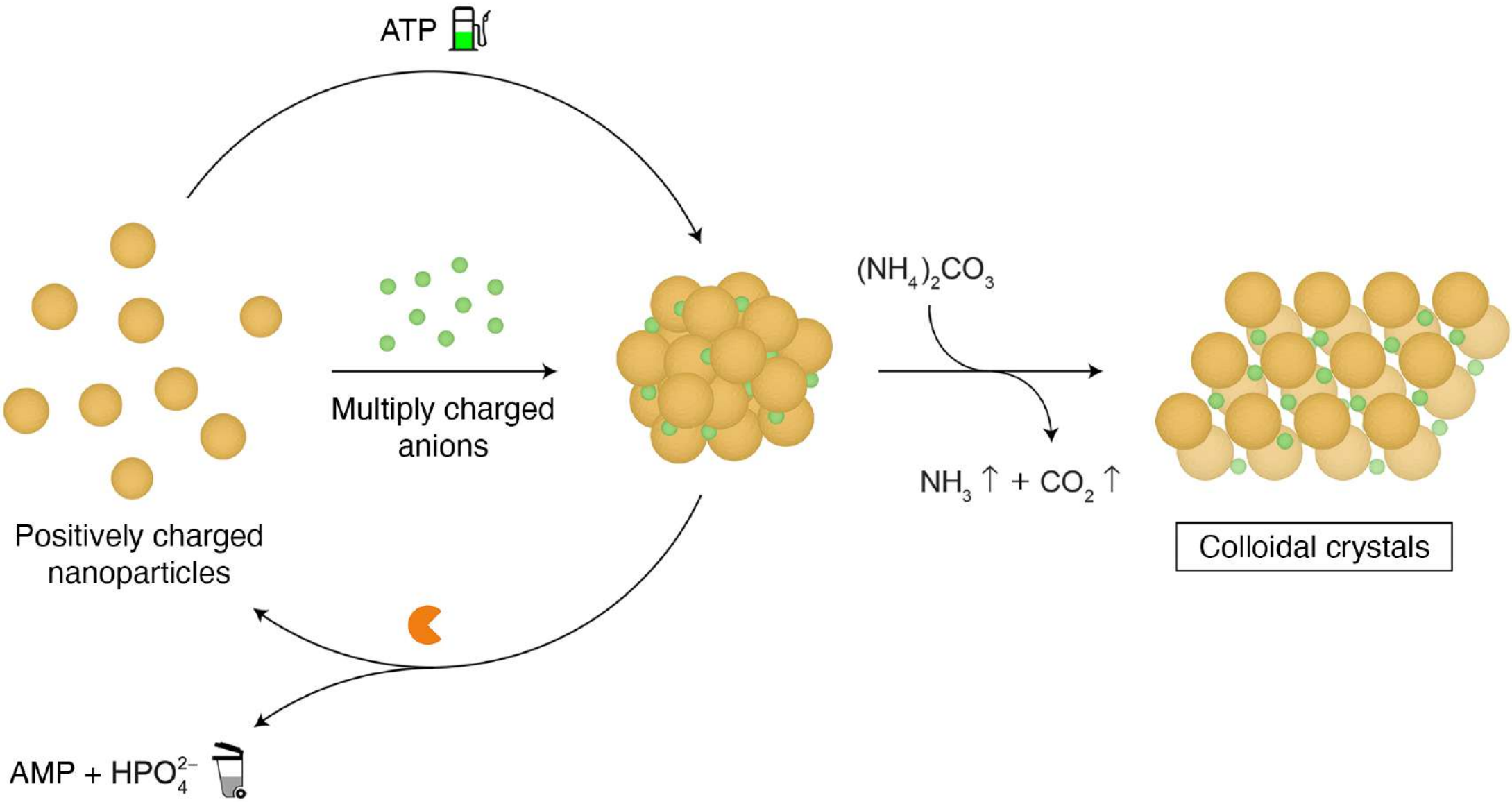
ATP
Multiply charged anions
Positively charged nanoparticles
$(NH_4)_2CO_3$
$NH_3 \uparrow + CO_2 \uparrow$
Colloidal crystals
$AMP + HPO_4^{2-}$